Chemical composition of carbonaceous asteroid Ryugu from synchrotron spectroscopy in the mid- to far-infrared of Hayabusa2-returned samples

Emmanuel Dartois, Yoko Kebukawa, Hikaru Yabuta, Jérémie Mathurin, Cécile Engrand, Jean Duprat, Laure Bejach, Alexandre Dazzi, Ariane Deniset-Besseau, Lydie Bonal, et al.

To cite this version:

Emmanuel Dartois, Yoko Kebukawa, Hikaru Yabuta, Jérémie Mathurin, Cécile Engrand, et al.. Chemical composition of carbonaceous asteroid Ryugu from synchrotron spectroscopy in the mid-to far-infrared of Hayabusa2-returned samples. Astronomy and Astrophysics - A&A, 2023, 671, 10.1051/0004-6361/202244702 . hal-04034487

HAL Id: hal-04034487
https://hal.science/hal-04034487v1

Submitted on 17 Mar 2023

A&A 671, A2 (2023)
https://doi.org/10.1051/0004-6361/202244702

Astronomy & Astrophysics

Chemical composition of carbonaceous asteroid Ryugu from synchrotron spectroscopy in the mid- to far-infrared of Hayabusa2-returned samples

Emmanuel Dartois[1], Yoko Kebukawa[2], Hikaru Yabuta[3], Jérémie Mathurin[4], Cécile Engrand[5], Jean Duprat[6], Laure Bejach[5], Alexandre Dazzi[4], Ariane Deniset-Besseau[4], Lydie Bonal[7], Eric Quirico[7], Christophe Sandt[8], Ferenc Borondics[8], Jens Barosch[9], George D. Cody[9], Brad T. De Gregorio[10], Minako Hashiguchi[11], David A. L. Kilcoyne[12], Mutsumi Komatsu[13,14], Zita Martins[15], Megumi Matsumoto[16], Gilles Montagnac[17], Smail Mostefaoui[6], Larry R. Nittler[9], Takuji Ohigashi[18], Taiga Okumura[19], Laurent Remusat[6], Scott Sandford[20], Miho Shigenaka[21], Rhonda Stroud[22], Hiroki Suga[23], Yoshio Takahashi[19,24], Yasuo Takeichi[24], Yusuke Tamenori[25], Maximilien Verdier-Paoletti[6], Shohei Yamashita[24], Tomoki Nakamura[16], Tomoyo Morita[16], Mizuha Kikuiri[16], Kana Amano[16], Eiichi Kagawa[16], Takaaki Noguchi[26], Hiroshi Naraoka[27], Ryuji Okazaki[27], Kanako Sakamoto[28], Hisayoshi Yurimoto[29,30], Masanao Abe[28], Kanami Kamide[21], Akiko Miyazaki[28], Aiko Nakato[28], Satoru Nakazawa[28], Masahiro Nishimura[28], Tatsuaki Okada[28], Takanao Saiki[28], Shogo Tachibana[19,28], Satoshi Tanaka[28], Fuyuto Terui[31], Yuichi Tsuda[28], Tomohiro Usui[28], Sei-ichiro Watanabe[32], Toru Yada[28], Kasumi Yogata[28], and Makoto Yoshikawa[28]

(Affiliations can be found after the references)

Received 5 August 2022 / Accepted 19 October 2022

ABSTRACT

Context. The current period is conducive to exploring our Solar System's origins with recent and future space sample return missions, which provide invaluable information from known Solar System asteroids and comets The Hayabusa2 mission of the Japan Aerospace Exploration Agency (JAXA) recently brought back samples from the surface of the Ryugu carbonaceous asteroid.
Aims. We aim to identify the different forms of chemical composition of organic matter and minerals that constitute these Solar System primitive objects, to shed light on the Solar System's origins.
Methods. In this work, we recorded infrared (IR) hyper-spectral maps of whole-rock Ryugu asteroid samples at the highest achievable spatial resolution with a synchrotron in the mid-IR (MIR). Additional global far-IR (FIR) spectra of each sample were also acquired.
Results. The hyper-spectral maps reveal the variability of the functional groups at small scales and the intimate association of phyllosilicates with the aliphatic components of the organic matter present in Ryugu. The relative proportion of column densities of the identified IR functional groups (aliphatics, hydroxyl + interlayer and/or physisorbed water, carbonyl, carbonates, and silicates) giving access to the composition of the Ryugu samples is estimated from these IR hyper-spectral maps. Phyllosilicate spectra reveal the presence of mixtures of serpentine and saponite. We do not detect anhydrous silicates in the samples analysed, at the scales probed. The carbonates are dominated by dolomite. Aliphatics organics are distributed over the whole samples at the micron scale probed with the synchrotron, and intimately mixed with the phyllosilicates. The aromatic C=C contribution could not be safely deconvolved from OH in most spectra, due to the ubiquitous presence of hydrated minerals. The peak intensity ratios of the organics methylene to methyl (CH_2/CH_3) of the Ryugu samples vary between about 1.5 and 2.5, and are compared to the ratios in chondrites from types 1 to 3. Overall, the mineralogical and organic characteristics of the Ryugu samples show similarities with those of CI chondrites, although with a noticeably higher CH_2/CH_3 in Ryugu than generally measured in C1 chondrites collected on Earth, and possibly a higher carbonate content.

Key words. minor planets, asteroids: individual: Ryugu – meteorites, meteors, meteoroids – methods: laboratory: solid state – techniques: imaging spectroscopy – techniques: spectroscopic – protoplanetary disks

1. Introduction

On the 6 December 2020, the Hayabusa2 mission of the Japan Aerospace Exploration Agency (JAXA) returned samples collected on the Cb-type dark asteroid Ryugu to Earth (Tsuda et al. 2020). For the first time, Hayabusa2 brought back samples from the surface of a known carbonaceous asteroid. These Solar System objects preserved ancient material that escaped planetary accretion and differentiation, providing pristine mineral and organic phases formed within the first million years after the proto-Sun gravitational collapse. The amount of material collected by Hayabusa2 (5.4 g) was larger than the 100 mg that had been expected (Tachibana et al. 2014; Sawada et al. 2017). The infrared (IR) analyses of these samples provide unprecedented information on the formation and early evolution of the Solar System and allow us to make the link between primitive interplanetary material and astronomical observations. A key goal of this study between the Organic Macromolecule (Yabuta et al. 2022) and Stone (Nakamura et al. 2023) sub-teams in the Hayabusa2 Initial Analysis is to elucidate the distributions and

Table 1. Ryugu samples analysed.

Sample	Region	Size (μm × μm)$^{(a)}$	#spectra /map
A0064−FO013	17-top-a	320 × 270	11 780
A0108−15	03-bot-a	130 × 130	2750
	03-bot-b	110 × 65	1100
	03-top-a	65 × 105	770
	03-top-b	65 × 70	506
	03-top-c	55 × 55	361
A0108−19	03-bot-a	260 × 300	8989
	03-top-a	260 × 300	9090
	b-bot-a	60 × 180	1323
	b-bot-b	35 × 80	620
	b-top-a	70 × 75	784
	b-top-b	90 × 125	1800
	b-top-c	75 × 100	1110
A0064−FO020	bot-a	130 × 100	1692
	top-a	125 × 50	1551
A0064−FO021	bot-a	140 × 185	4440
	top-a	55 × 100	1014
A0106−13	bot-a	185 × 240	6336
	top-a	110 × 30	574
	top-b	50 × 45	360
C0046−FO004	10-bot-a	55 × 110	1025
	10-top-a	60 × 110	1189
	10-top-b	70 × 70	1$^{(b)}$
C0002−FC016	bot-a	130 × 130	2805
	top-a	140 × 130	2352
C0040−FC025	bot-a	417 × 393	18209
	bot-b	192 × 246	5248
C0109−4	bot-a	200 × 190	5250
	top-a	200 × 200	5256
C0109−10	bot-a	180 × 180	5767
	top-a	200 × 200	5110
C0057−5	bot-a	40 × 65	391
	bot-b	80 × 110	999$^{(c)}$
	bot-c	40 × 45	289
	bot-d	40 × 40	240

Notes. $^{(a)}$Projected size (flattened on the diamond window). $^{(b)}$No map, global spectrum over the size mentioned. $^{(c)}$Measured but not used because of contamination suspicion of part of the map with a deposited small dust particle during measurements.

chemical characteristics of macro-molecular organic materials and minerals in a C-type asteroid. In this work, we provide hyper-spectral analyses showing the characteristic content and distribution of both organics and minerals of Hayabusa2-returned particles that will enable the comparison with other types of asteroidal and cometary samples available in the laboratory.

2. Experiments

2.1. Sample preparation

The Ryugu samples originated from chamber A and chamber C, respectively collected for the former at the surface of the first touchdown site and potentially containing sub-surface material ejected from the Hayabusa2-made artificial crater for the later (Tachibana et al. 2022). The studied samples include fragments of individual particles from A0064, C0002, C0040, C0046, and C0057 as well as aggregate samples from A0106-13, A0108-15, A0108-19, C0109-4, and C0109-10 (see Table 1). In total six fragments from chamber A and six from chamber C were prepared for Fourier Transform IR micro-spectroscopy (μ-FTIR), in particular for pre-characterisation before IR nanospectroscopy (AFM-IR Mathurin et al. 2022a,b; Dazzi & Prater 2017). Each fragment was micro-manipulated and transferred into a diamond compression cell made of two facing diamond windows. The fragments were flattened to a thickness of $\sim$1 μm in order to provide an optimal thickness for IR spectroscopic transmission measurements. After compression in the diamond cell, the flattened sample was distributed generally in each diamond window, providing two complementary flat samples, named ‘top’ and ‘bottom’, depending on the diamond window in which the sample finally resided. In some cases the majority of the sample remained in one diamond window only.

2.2. Synchrotron MIR and FIR measurements

The transmission IR measurements were performed on the SMIS beamline at the synchrotron SOLEIL during three runs in July and October 2021, and in April 2022. Table 1 presents the names of the samples analysed both in the mid-IR (MIR, 4000–700 cm^{-1}) and the far-IR (FIR, 700–100 cm^{-1}), their approximate size once flattened, and the number of pixels in the recorded hyper-spectral IR maps. The synchrotron beam was coupled to a Nicolet continuum IR microscope, flushed under dry nitrogen at room temperature. For the measurements presented in this analysis, the IR spot size was optimised close to the diffraction limit, with a 6 μm × 6 μm sampling window, and maps were recorded using orientations adapted to the geometry of each Ryugu fragment. The map sampling step was 3 μm (Nyquist sampling). In order to better constrain the mineral components of the Ryugu samples, additional FIR spectra were recorded on a Nicolet Nic-Plan IR microscope using a bolometer, with spot sizes usually covering the entire size of the considered particles. Additional measurements over the entire size of the considered particles were also conducted on another Nicolet continuum IR microscope at ISMO, with a conventional Globar IR source covering an extended MIR range from 4000 cm^{-1} down to about 450 cm^{-1}, ensuring the good behaviour in the overlapping 700–450 cm^{-1} spectral region. The FIR spectra were stiched to the MIR spectrum when necessary by applying a gain correction factor of typically a few percent, to build the global individual grain spectra covering the 4000–100 cm^{-1} range. The synchrotron IR beam μ-spectrometry was mandatory to sample the small components (e.g. small carbonate components) present in the samples, and to evaluate their spatial distribution and individual sizes, in order to build analytical chemical maps. The synchrotron hyper-spectral maps acquired on each Ryugu sample were used with the following complementary approaches: (i) the spectra corresponding to each map pixel were decomposed into individual contributions corresponding to specific vibrational modes (as shown in Figs. 1 and 2), to produce false-colour images of the spatial distribution of the different components (as shown, for instance, in Figs. 3 and 4); (ii) an average global spectrum (Fig. 5) was calculated for each map of the Ryugu samples combining the best signal-to-noise MIR (either synchrotron average map or Globar source) and FIR spectra, to estimate the CH$_2$/CH$_3$ ratios (Figs. 6–8) and the distribution of the different

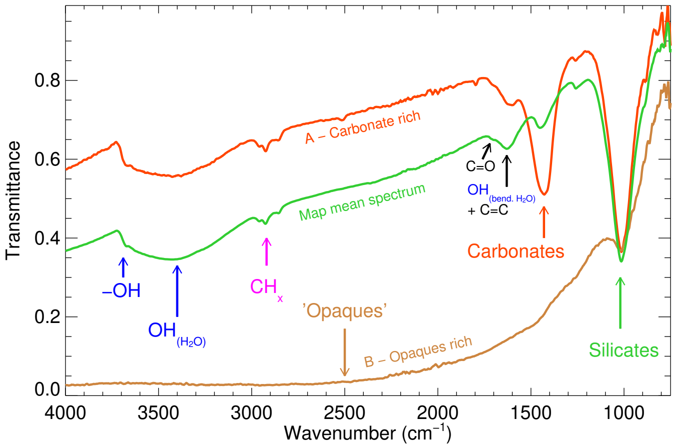

Fig. 1. Representative Ryugu sample A0108-15 transmittance spectra (6 × 6 μm spots) showing a carbonate-rich region (A), a region with inorganic 'opaques' (probably magnetite and/or Fe sulphides) (B), and the map average spectrum (green) corresponding to map 1 reported in Fig. 3. Vibrational modes of interest (including the ones used to build the coloured maps such as in Fig. 3) are shown with arrows.

components in each map (Fig. 9), as well as the proportion of carbonates to phyllosilicates (Fig. 10).

2.3. AFM-IR measurements

An IR map at the tens of nanometres resolution was obtained using AFM-IR (shown in the lower left panel of Fig. 3), a technique combining an Atomic Force Microscope (AFM) to a tunable IR laser. It is based on the detection, by the AFM probe, of the photo-thermal expansion that occurs in the sample after IR absorption of the material located just under the AFM tip (Dazzi et al. 2005). The AFM-IR system was a NanoIR2 from Anasys Instruments (Bruker) coupled to a multi-chip Quantum Cascade Laser (QCL, Daylight Solutions) covering the MIR range from 900 cm^{-1} up to 1960 cm^{-1}. An Au-coated silicon AFM tip was used (Budget sensors, tap 300). The AFM-IR was used in tapping mode (Mathurin et al. 2020, 2019). The IR map (AFM image of 30 μm × 30 μm, 1000 × 1000 pixels) was acquired at fixed tuned laser wavenumbers: 1020, 1420, and 1900 cm^{-1}, corresponding to the absorption of silicate and carbonate chemical groups, and of the continuum, respectively. The IR mapping acquisitions were made using a 0.1 Hz scan rate with a laser power of 56.26% of the QCL chip, a repetition rate of 1340 kHz, and a pulse width of 120 ns. These maps were combined in a composite three-colour RGB image (green at 1020 cm^{-1}, blue at 1420 cm^{-1}, and red at 1900 cm^{-1}), shown in the lower left panel of Fig. 3. Before combining the maps, minor AFM stripping was corrected by interpolation, the maps were realigned to the 1020 cm^{-1} map using their topographic AFM maps, and they were slightly smoothed using a 5-pixel kernel. To maximise the contrast in the composite image for bands with different intrinsic intensities, the intensity of each image recorded at a given wavenumber was first normalised to its maximum intensity over the entire map before the images were combined.

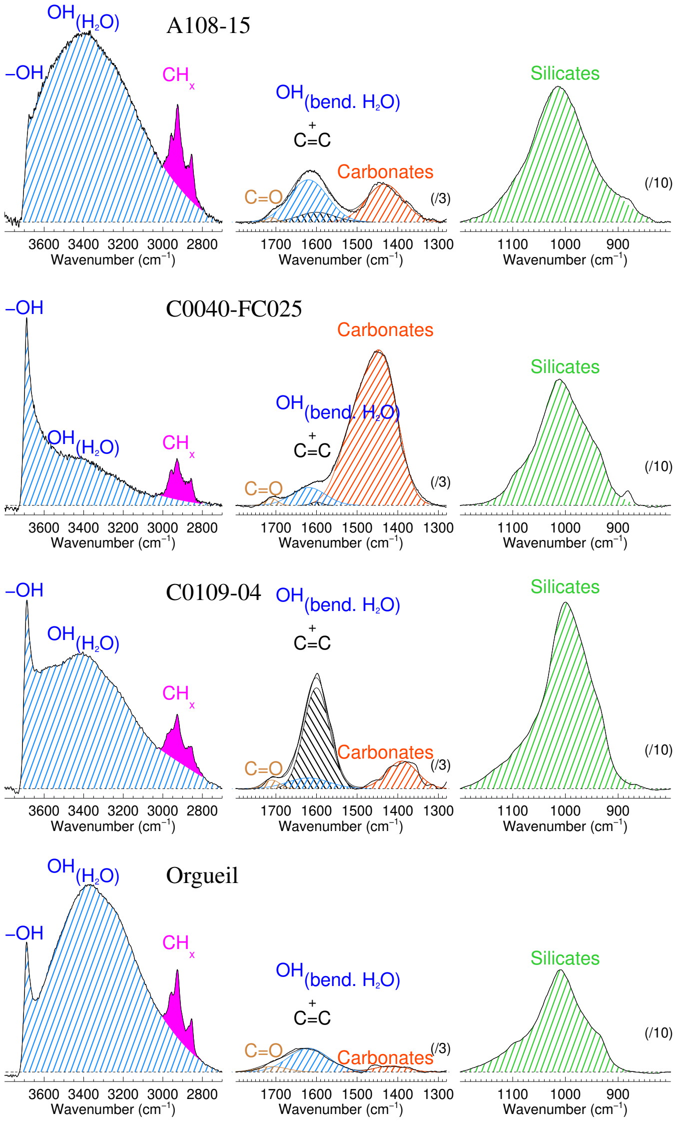

Fig. 2. Close-up and deconvolution of the individual bands for the global spectra (corresponding to the maps of Figs. 3 and 4) recorded for sample A0108-15 (03-top-a), upper spectrum, with a high physisorbed and/or interlayer water contribution, and C0040-FC025 (bot-b), second spectrum from top, dominated by the OH hydroxyl contribution. Individual bands are represented by hatching: OH stretch (blue in the 3000–3700 cm^{-1} region), CH stretch (magenta), C=O carbonyl stretch (brown), OH bending (blue around 1640 cm^{-1}), aromatic C=C bending (black), carbonates (red), and silicates (green). Each wavenumber range is normalised with regard to the high wavenumber range by a factor (indicated in parenthesis) for clarity of the deconvolution. The spectrum of a particularly C-aromatic-rich grain, C0109-04 (top-a), is also shown. For comparison, a spectrum taken from Orgueil, which was prepared and recorded in the same conditions as the Ryugu samples, is shown at the bottom. See text for details.

3. Analyses and results

Each spectrum in the synchrotron hyper-spectral maps was baseline corrected. The integrated optical depths over several absorption bands of interest were calculated, and divided by their corresponding integrated absorption cross section to estimate the column density measured in each pixel of the maps. The resulting maps with significant signal-to-noise ratios correspond to the silicate's SiO stretching mode, CO_3 carbonates, OH stretching mode, and aliphatic CH. In addition, we built a map on phases that do not exhibit specific absorption bands but a wider light scatter and/or absorption behaviour that can be referred to as 'opaques'. For these opaque phases, instead of measuring a particular band, we monitored the non-baseline-corrected

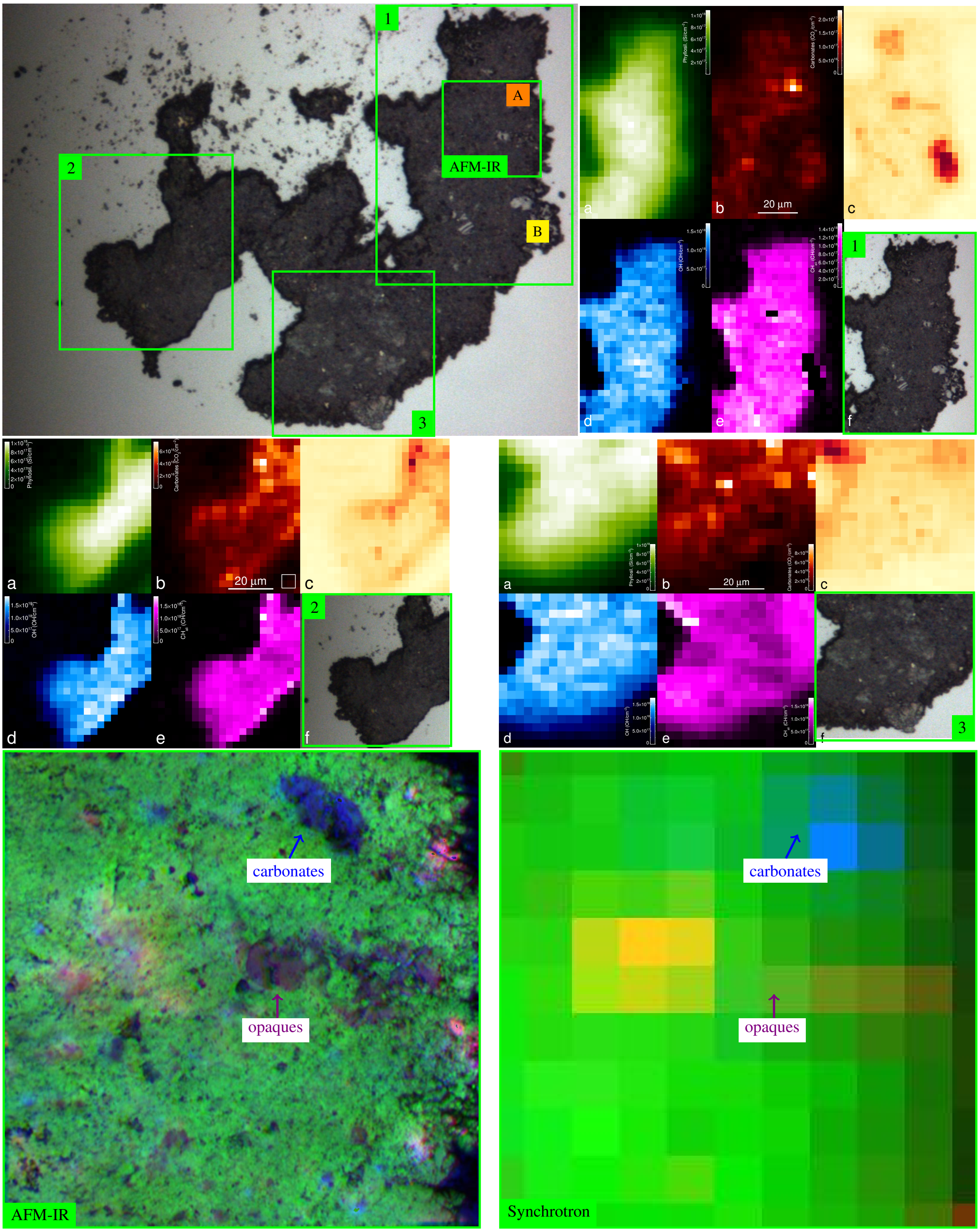

Fig. 3. Chamber A Ryugu sample #A0108-15 (03) (top diamond window). Upper left: Visible image recording the entire flattened grain with an extent of about 150 μm. The positions A and B correspond to the individual spectra shown in Fig. 1, showing a carbonate-rich region (A) and a region with inorganic opaques (probably magnetite and/or Fe sulphides) (B). The regions of interest mapped with the synchrotron measurements are numbered from 1 to 3. Top right and middle panel sets: Coloured phase maps for regions 1 to 3 corresponding, for each map, to silicates (a, green), carbonates (b, red), opaques, (c, yellow-orange), OH stretch (d, blue), CH stretch (e, magenta), and respective visible image (f). It should be noted that a few outlier (white) points with apparent high optical depth may be observed in the OH and CH stretch maps. They coincide with the presence of opaques or are on maps' borders. They are due to low signal-to-noise ratios, which lead to a higher uncertainty on the baseline determination (and correction). Lower panel: Images representing the same region mapped by AFM-IR (left, composite map of 30 μm $\times$ 30 μm, green, silicates; blue, carbonates; red, opaques), and mapped with synchrotron at the highest achievable spatial resolution (right, $\sim$6 μm aperture with a step size of $\sim$3 μm, i.e. close to Nyquist sampling).

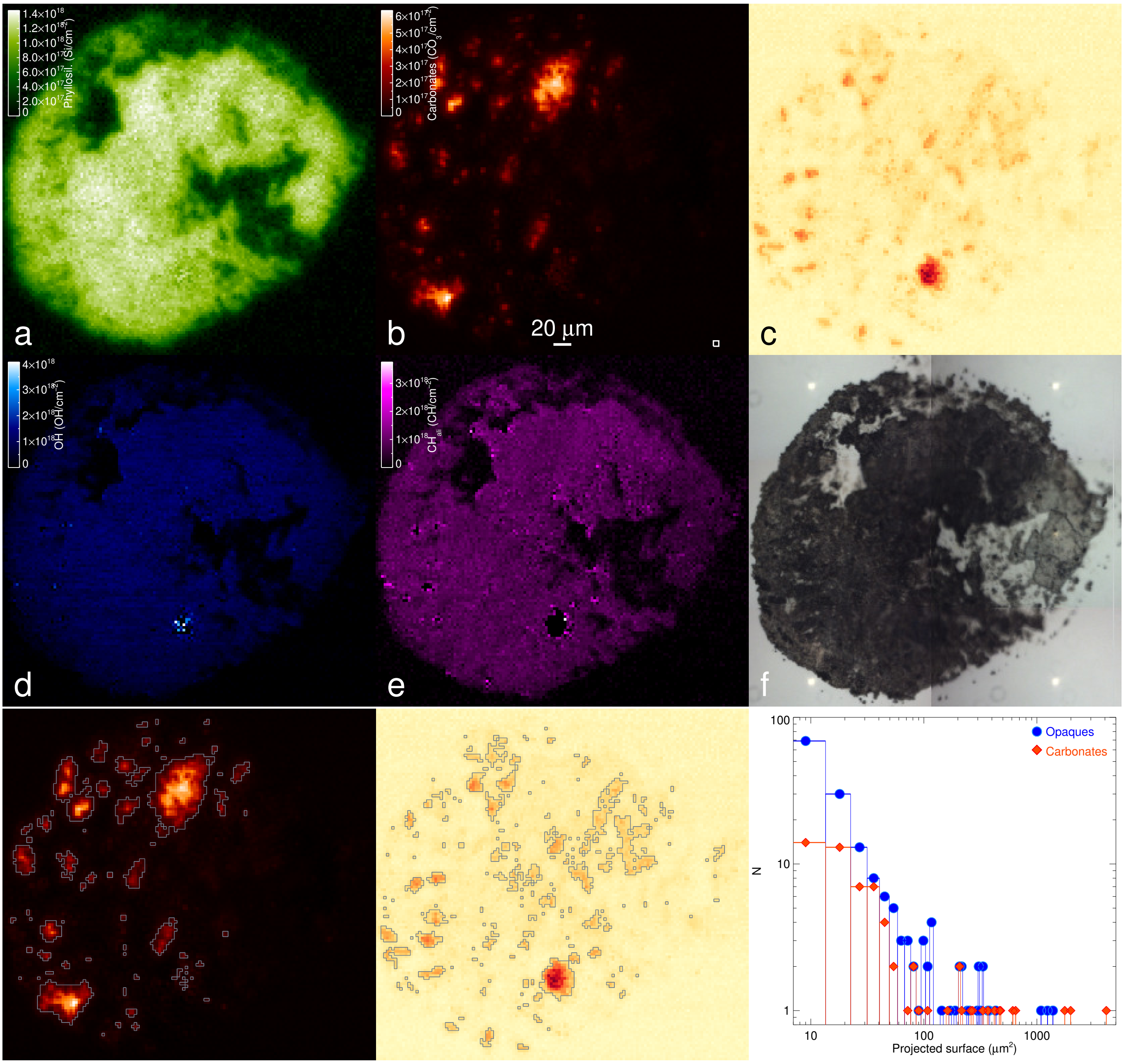

Fig. 4. Chamber C Ryugu sample C0040-FC025 (bottom diamond window). Phase maps of silicates (a, green), carbonates (b, red), opaques (c, yellow-orange), OH stretch (d, blue), CH stretch (e, magenta), and corresponding visible images (f). Bottom: images representing the edge detection of individual ROIs based on the intensity map of carbonates (left), and of opaques (middle), and resulting size distribution histograms (right). The x-axis represents the projected surface of each region in µm^2 (multiples of the spatial resolution of 9 µm^2). As the samples are flattened to ~1 µm, this projected surface is directly proportional to the same volume value.

continuum drop by comparing the optical depth difference between the continuum on the right side of the silicates (i.e. at about 800 cm^{-1}) and in an IR absorption-free region at about 2500 cm^{-1}. These opaques maps betray the presence of species such as magnetite and/or sulphides, as these phases do not display specific signatures in the MIR range, but strongly absorb and/or scatter the IR beam.

The adopted integrated absorption cross sections (also called band strengths) are given in Table A.1. We detail below how they were determined from literature optical constants and/or spectra.

3.1. Band strengths

An integrated absorption cross section can be evaluated from the imaginary part of the optical constants for a given solid by integrating over a vibrational band:

$$\mathcal{A}(\mathrm{cm/[group]}) = \int_{\bar{\nu}_{\min}}^{\bar{\nu}_{max}} \frac{\tau(\bar{\nu})\mathrm{d}\bar{\nu}}{N} = \int_{\bar{\nu}_{\min}}^{\bar{\nu}_{\max}} \frac{4\pi k\bar{\nu}\times\mathrm{thickness}\times\mathrm{d}\bar{\nu}}{N} = \int_{\bar{\nu}_{\min}}^{\bar{\nu}_{\max}} \frac{4\pi k\bar{\nu}\mathrm{d}\bar{\nu}\times M}{N_{\mathrm{A}}\times\rho\times n_{group}}, \quad (1)$$

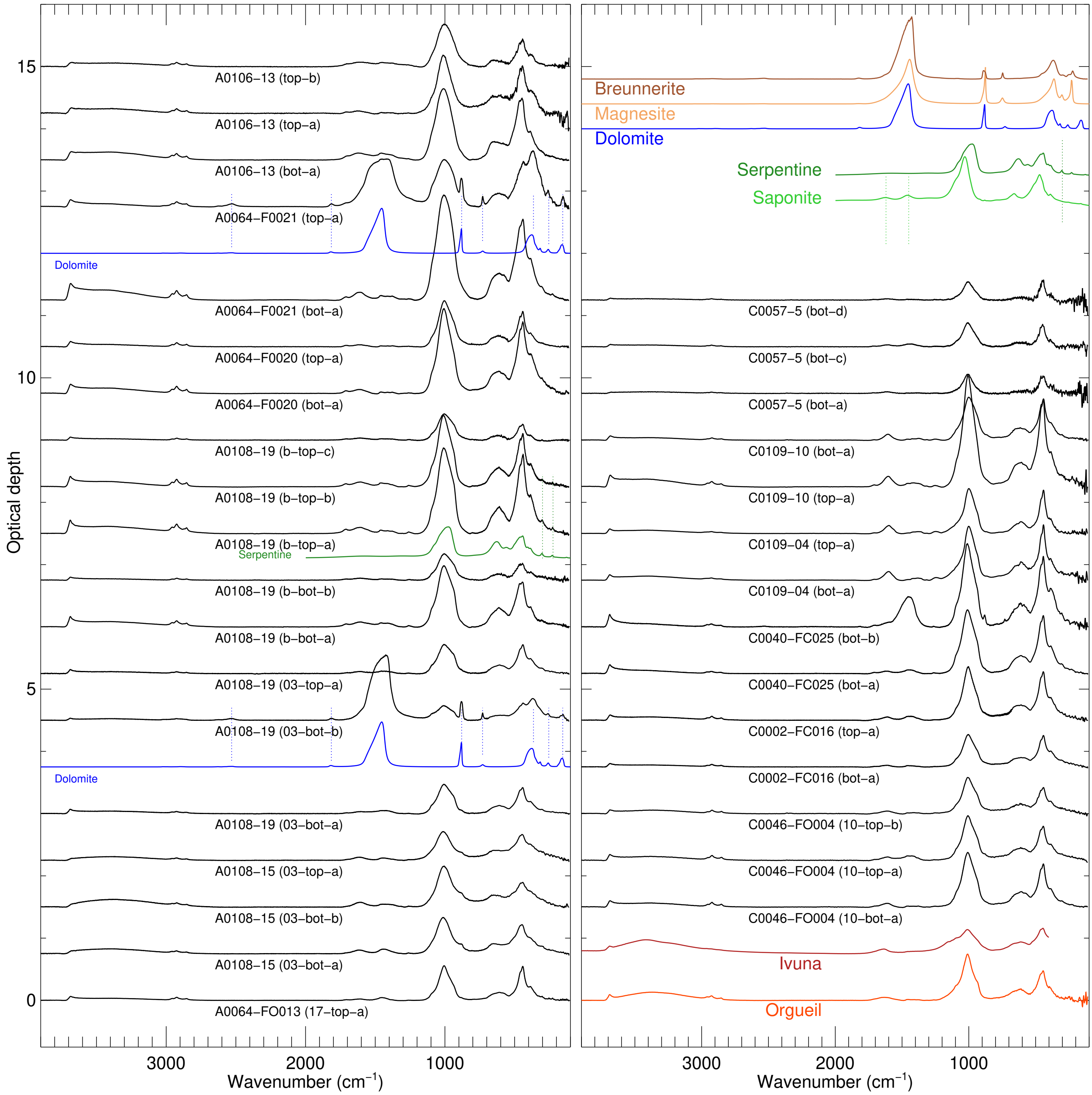

Fig. 5. Global MIR to FIR spectra of the grains analysed, including large regions of interest for some of the grains from chamber A (left) and chamber C (right). Reference spectra for major species identified in the Ryugu samples spectra such as carbonates: dolomite, Roush (2021); magnesite, Roush (2021); breunnerite $Mg_{0.78}Fe_{0.22}CO_3$, (this work) and phyllosilicates: saponite, serpentine, Glotch et al. (2007), are displayed for comparison (mineral compositions are given in Table A.1). For some grains with a large carbonate contribution to the spectrum, we also display the spectrum of dolomite, the carbonate the closest to the measured band positions and intensities. In addition, in the lower right panel are displayed the spectra of two CI1 meteorites closely related to the composition of the Ryugu samples, Orgueil (this work, measured under the same conditions in a diamond cell) and Ivuna (measured in a KBr pellet at 300°C, from Beck, Pierre (2012): MIR absorbance spectra of bulk CI chondrites in KBr pellets at ambient temperature, 150°C and 300°C. SSHADE/GhoSST, OSUG Data Center, https://doi.org/10.26302/SSHADE/EXPERIMENT_LB_20170719_001).

where $\tau(\bar{\nu})$ is the optical depth of the vibrational band related to the group, N the column density of the considered group, $M\,[\mathrm{g\,mol^{-1}}]$ is the molar mass, N_A the Avogadro number, $\rho(\mathrm{g\,cm^{-3}}$ the volumetric mass density, n_{group} the number of groups considered in the calculated molar mass to which $\mathcal{A}$ is normalised (e.g. for dolomite, if M is calculated with the formula $CaMg(CO_3)_2$, and $\mathcal{A}$ is expressed per CO_3 group, then $n_{CO_3} = 2$).

OH band strength

In Ryugu phyllosilicates, in addition to the OH relatively sharp hydroxyl group at about 3700 cm^{-1}, some of the recorded

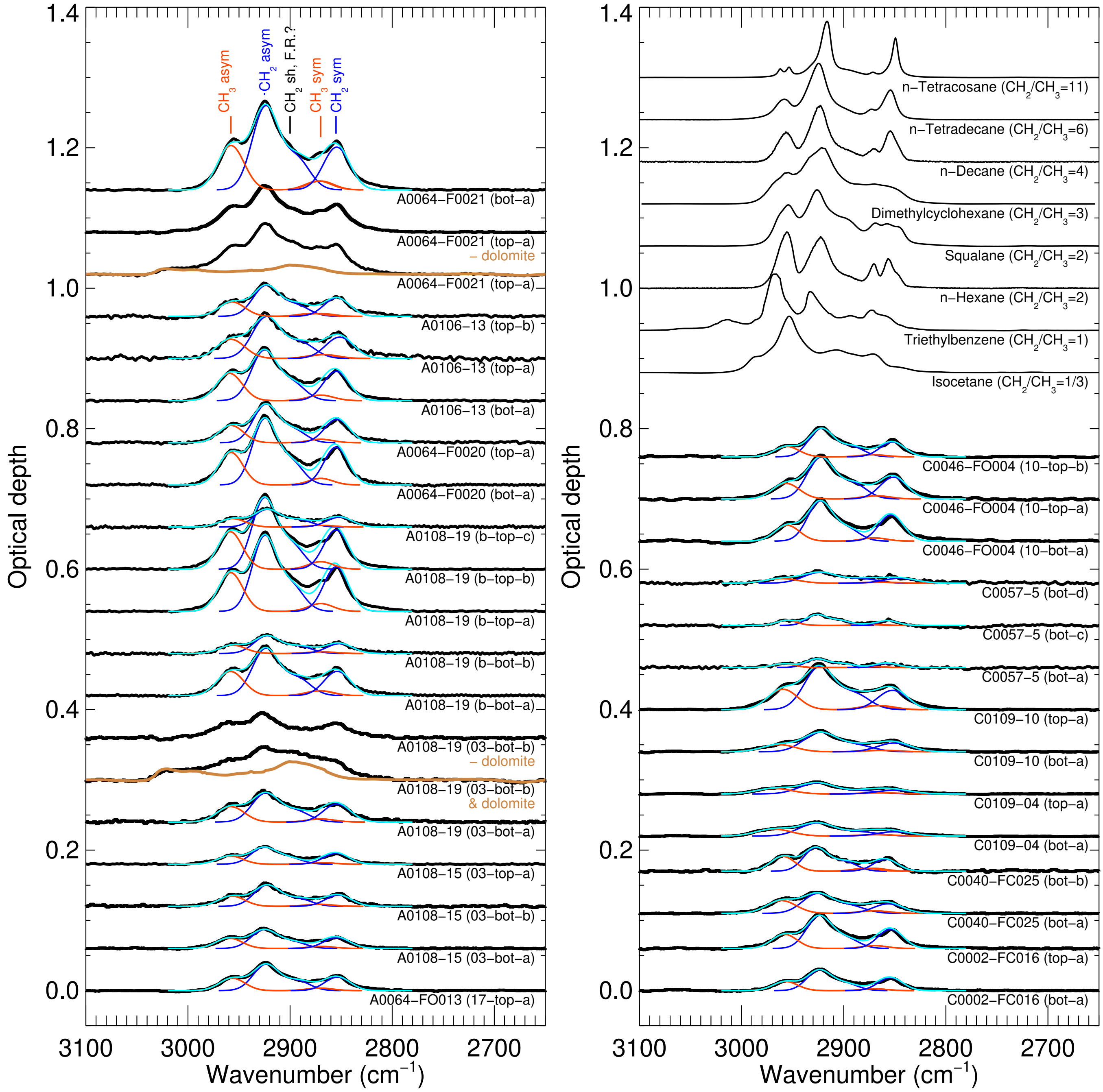

Fig. 6. Aliphatic stretches' spectral decomposition used to calculate the methylene-to-methyl ratios. The spectra are fitted with five components corresponding to the asymmetric CH_3 stretching mode (~2960 cm^{-1}), the asymmetric CH_2 stretch and its red shoulder (~2920–2900 cm^{-1}), and the symmetric stretches of the same groups ~2880–2850 cm^{-1}). The approximate positions of these modes are labelled above the upper left spectrum. The CH_3 contributions are shown in red, and the CH_2 ones in blue. In a few spectra, a contribution from dolomite affects the profile. For these, the expected dolomite spectrum contribution is shown in brown and the dolomite-subtracted spectrum is shown above. Spectra with a high fraction of dolomite contribution were not deconvolved. In the upper right corner are shown reference spectra of linear and branched alkanes, an alkyl benzene and a cycloalkane, with varying methylene-to-methyl ratios: isocetane, squalane, *n*-tetradecane (purchased from Merck), and *n*-tetracosane (provided by Sylvie Heron) were measured as received with our FTIR-microscope; *n*-hexane and n-decane spectra are from Dartois et al. (2004); triethylbenzene and dimethylcyclohexane spectra are from the NIST database: `https://webbook.nist.gov/chemistry/`. Although they are specific species, this series shows the expected asymmetric CH_2/CH_3 stretch band ratio trend.

spectra show a broad band centred at about 3300 cm^{-1} for interlayer water, with some contribution arising from residual ambient water physisorption in some cases. For these last modes, in the stretching mode region, we adopted the band strength of liquid water (see Table A.1). The estimate of the OH stretching was used to estimate the contribution in the MIR region of the OH bending mode, overlapping with aromatic C=C modes. In liquid water, the OH bending to OH stretching mode band strength ratio is about 0.072. This ratio was estimated also using natural saponite spectra recently published in a review (Kloprogge & Ponce 2021), leading to 0.071 ± 0.0017.

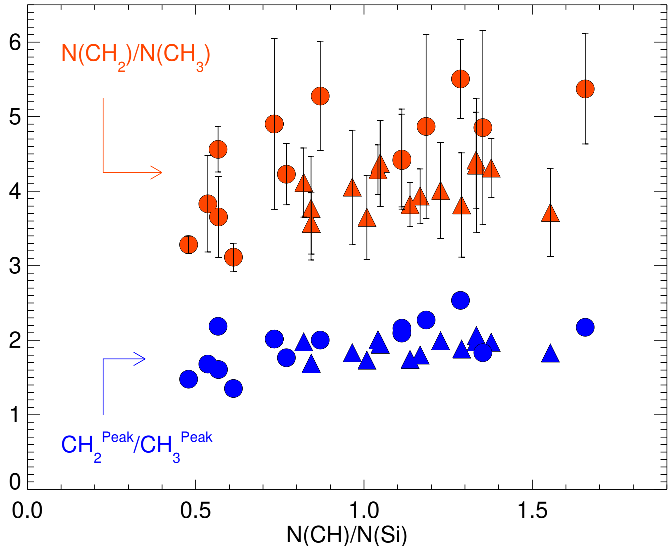

Fig. 7. Methylene-to-methyl (CH_2/CH_3) ratios (chamber A: triangles; chamber C: circles) expressed as the asymmetric stretching mode peak maximum intensity (blue) and as column density ratio (red), derived from the deconvolution of the aliphatic bands, as a function of the CH-to-Si column density ratio. See text for details.

Aliphatic CH band strength

The individual contributions to the observed profile in the CH stretching mode region for the methyl and methylene groups' asymmetric and symmetric vibrations have been discussed in the context of interstellar organics, based on laboratory experiments (Dartois et al. 2004, 2007) and literature data referenced therein. In addition, as discussed hereafter, a global band strength per CH can be calculated and used when the observed band is not deconvolved into its individual specific vibrations. They are given in Table A.1

C=C band strength

The (poly)aromatic C=C band strength may vary depending on their chemical speciation. The closest material to use as a reference is probably the insoluble organic matter (IOM) from meteorites (e.g. Kebukawa et al. 2011; Orthous-Daunay 2013). Using IOM spectra from Fig. 2 of Orthous-Daunay (2013), for which the H/C ratio has been measured independently (Alexander et al. 2007), provides a way to determine such C=C band strength. The IOM carbon content is dominated by carbon involved in aliphatic, aromatic, and carbonyl functional groups. The measured column density of C is thus given by the sum of these individual contributions:

$$N_C = N_C^{\text{aliph.}} + N_C^{\text{aro.}} + N_C^{\text{carbonyl}} = \gamma\, N_H^{aliph.} + \frac{\int \tau_{C=C} d\bar{\nu}}{\mathcal{A}^{Aro.}_{C=C}} + \frac{\int \tau_{C=O} d\bar{\nu}}{\mathcal{A}_{C=O}}, \quad (2)$$

where $\mathcal{A}^{\text{Aro.}}_{\text{C=C}}$ is the integrated absorption cross section for aromatic carbons, per C; $\mathcal{A}_{\text{C=O}}$ for the carbonyl group, per C. γ is the factor linking the CH aliphatic hydrogen column density to the aliphatic carbon one. This factor is linked to the methylene-to-methyl ratio $\beta = N_{CH_2}/N_{CH_3}$, defining the mean number of hydrogen per C in the aliphatic stretching mode region. From β, one derives that $\gamma = (\beta + 1)/(2\beta + 3)$. To first order, one can neglect the carbonyl C=O contribution to the carbon budget, as the measured C=O band integrated optical depth (of the same order as the C=C band in the IOM spectra) is only due to an intrinsically high $\mathcal{A}_{\text{C=O}}$ compared to that of C=C, implying a much lower C contribution. The γ parameter typically varies only from 0.40 to 0.46 for $N_{CH_2}/N_{CH_3} = 1$ to 5, and, in the absence of the exact knowledge of the β ratio, one can adopt $\gamma = 0.43 \pm 0.03$ to cover the range of most observed IOM values.

The IOM spectra show that the organic hydrogen content is dominated by aliphatic CHs, with methyl (CH_3) and methylene (CH_2) bonds. The measured aliphatics hydrogen column density on a spectrum is then given by:

$$N_{\text{H}}^{\text{aliph.}} = 3N_{CH_3} + 2N_{CH_2} = 3\frac{\int \tau^{\text{asym}}_{\text{CH}_3} \text{d}\bar{\nu}}{\mathcal{A}^{\text{asym}}_{\text{CH}_3}} + 2\frac{\int \tau^{\text{asym}}_{\text{CH}_2} \text{d}\bar{\nu}}{\mathcal{A}^{\text{asym}}_{\text{CH}_2}}. \quad (3)$$

To a good approximation (Dartois et al. 2004, 2007),

$$\mathcal{A}^{\text{asym}}_{\text{CH}_3}/3 \approx \mathcal{A}^{\text{asym}}_{\text{CH}_2}/2 \approx 4 \times 10^{-18} \text{cm/H} = \mathcal{A}_{\text{CH}} \quad (4)$$

and

$$\mathcal{A}^{\text{sym}}_{\text{CH}_3}/\mathcal{A}^{\text{asym}}_{\text{CH}_3} \approx \mathcal{A}^{\text{sym}}_{\text{CH}_2}/\mathcal{A}^{\text{asym}}_{\text{CH}_2} \approx 0.2, \quad (5)$$

so that

$$\text{N}_{\text{H}}^{\text{aliph.}} \approx \frac{\int_{\bar{\nu}_{2800}}^{\bar{\nu}_{3000}} \tau_{\text{aliph}} \text{d}\bar{\nu}}{1.2\mathcal{A}_{\text{CH}}}. \quad (6)$$

Then, with $\text{C/H} \approx N_{\text{C}}/N_{\text{H}}^{\text{aliph.}}$, the integrated absorption strength of aromatic C can be derived as

$$\mathcal{A}^{\text{Aro.}}_{\text{C=C}} \approx \frac{\int \tau_{\text{C=C}} \text{d}\bar{\nu}}{\int_{\bar{\nu}_{2800}}^{\bar{\nu}_{3000}} \tau_{\text{aliph}} \text{d}\bar{\nu}} \times 1.2\mathcal{A}_{\text{CH}} \Big/ \left(\frac{\text{C}}{\text{H}} - \gamma\right). \quad (7)$$

Reanalysing data from several IOM measurements from Fig. 8 in Orthous-Daunay (2013), which reports the correlation between the ratio of integrated absorption of the CH stretching modes over the aromatic C=C one versus the H/C ratio, $\int_{\bar{\nu}_{2800}}^{\bar{\nu}_{3000}} \tau_{\text{aliph}} \text{d}\bar{\nu} / \int \tau_{\text{C=C}} \text{d}\bar{\nu} \approx \text{H/C}$, over the H/C range of about 0.35 to 0.8. Putting this correlation into Eq. (7) and normalising per carbon atom (i.e. specifying that each C=C contributes for two carbon atoms), one deduces:

$$\mathcal{A}^{\text{Aro.}}_{\text{C=C}}(\text{IOM}) \approx 3.2 \pm 0.4 \times 10^{-18} \text{cm/C}. \quad (8)$$

Carbonate CO_3 band strength

The CO_3 asymmetric stretches from dolomite, magnesite, and calcite carbonates were calculated based on the optical constants from Roush (2021). We assumed a generic band strength of 2×10^{-16} cm/CO_3.

Silicate SiO band strength

The silicates' SiO stretching mode band strengths for saponite and serpentine were obtained from the analyses of optical constants from Glotch et al. (2007); Roush et al. (1991); Mooney & Knacke (1985). We assumed a generic band strength of 1.4×10^{-16} cm/Si.

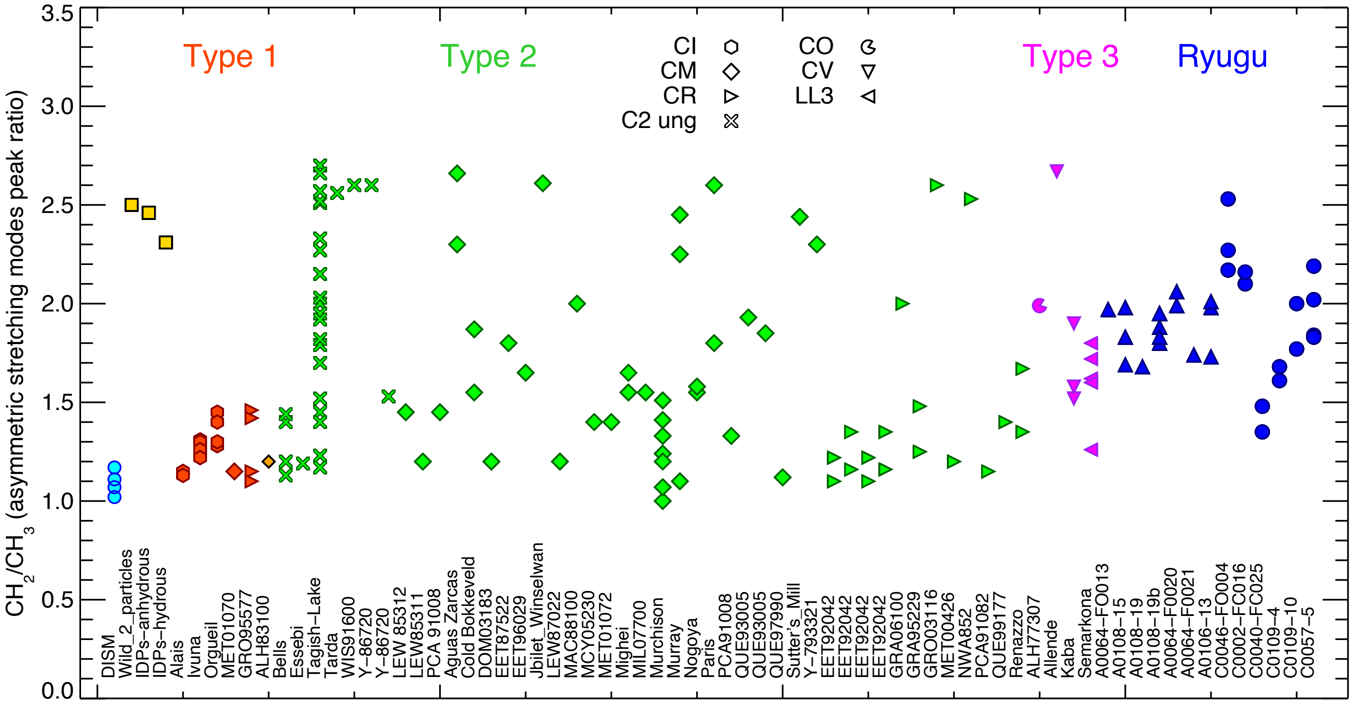

Fig. 8. Comparison of methylene-to-methyl (CH_2/CH_3) intensity peak ratios for Ryugu bulk sample measurements (this work) with measurements from the literature for diffuse ISM observations (Sandford et al. 1991; Pendleton et al. 1994; Dartois et al. 2007; Godard et al. 2012), Stardust samples (comet 81P/Wild2, Keller et al. 2006), IDPs (Flynn et al. 2003), and meteorites bulk and IOM samples (Alexander et al. 2014; Briani et al. 2013; Dionnet et al. 2018; Kebukawa et al. 2010, 2011, 2019; Kerraouch et al. 2022; Merouane et al. 2012; Orthous-Daunay 2011, 2013; Quirico et al. 2018; Yesiltas et al. 2014, 2015, 2022; Yesiltas & Kebukawa 2016).

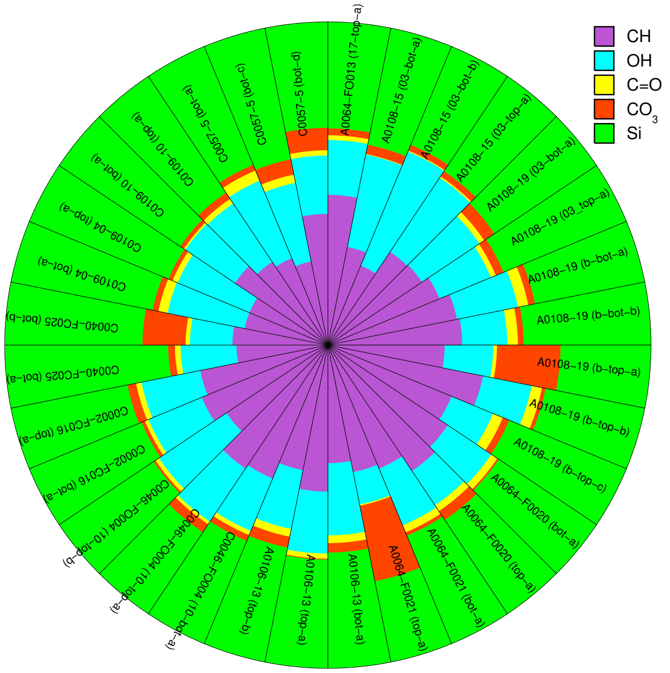

Fig. 9. Relative proportions of the different functional groups (aliphatics, hydroxyl + interlayer and/or physisorbed water, carbonyl, carbonates, and silicates) from the FTIR analysis of the different samples, shown per functional group CH, OH, C=O, CO_3, and Si, respectively.

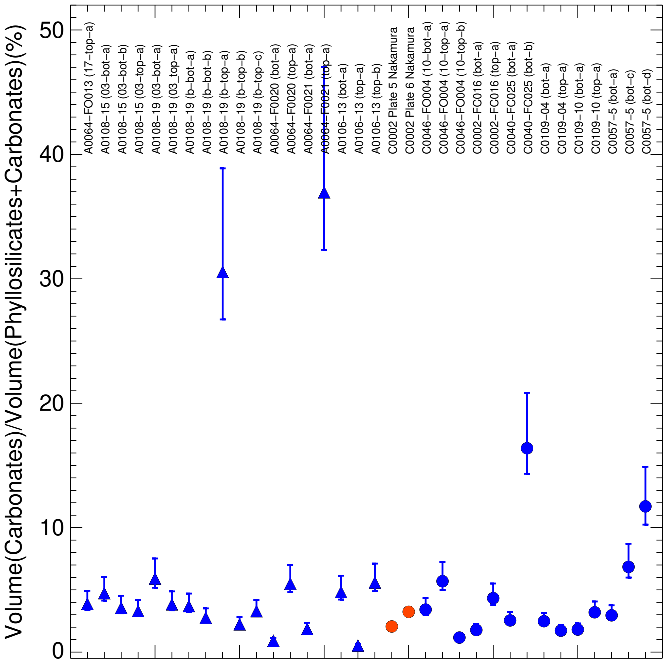

Fig. 10. Relative volume ratio of carbonates to (carbonates + phyllosilicates) in the Ryugu samples (in %), calculated using Eq. (13). Samples from chamber A are plotted as blue triangles and chamber C samples are represented as blue dots (see text for details). Two measurements on polished sections of chamber C samples are reported for comparison as filled red dots (Table S6 of Nakamura et al. 2023).

3.2. Phase maps

The phase maps computed from the integration of band vibrations in the synchrotron hyper-spectral maps for one sample from chamber A (A0108-15) and one from chamber C (C0040-FC025) are shown in Figs. 3 and 4, respectively. All the other measured chamber A and C samples' phase maps are shown in the appendix. These two maps exemplify the typical information obtained with the performed synchrotron measurements. In all recorded maps, both the phyllosilicates and aliphatics components of the organics are widespread. They are present everywhere at the scale probed with the synchrotron (6 µm), sampled at 3 µm steps, and intimately mixed at such a scale. The organic aromatic C=C component is ubiquitous in the Ryugu samples (as seen in Raman spectra, e.g. Bonal et al. 2022). However, the corresponding signal in the FTIR spectra overlaps with that of the OH bending mode from interlayer water, which is significant in the case of Ryugu spectra. Therefore, no maps for the aromatic C=C were extracted in this work, and this component is discussed in more detail in Sect. 3.5. Physisorbed and interlayer water, observed through the OH stretching modes, is also observed at varying degrees. Carbonates and opaques (magnetite and/or sulphides) show a different behaviour. Image processing analyses are shown in Fig. 4 for the opaques and carbonate maps. Individual regions of interest (ROIs) were automatically detected by thresholding the images and deriving individual non-connected projected surfaces. These 2D projected surfaces correspond to probing initial 3D volumes flattened to about one micron in thickness. A histogram of the ROI size distribution is shown in the right panel of Fig. 4. The opaques distribution for these grains show a size distribution following, to first order, the inverse of their volume. The carbonate distribution is different, with fewer small grains than for opaques, and individual large carbonate grains with projected surfaces as large as a few thousand µm^2. These correspond to individual carbonate grains of tens of microns in diameter prior to flattening, as also observed by Yokoyama et al. (2023) and Nakamura et al. (2023).

The AFM-IR measurements extend the analysis to small scales around a few tens of nanometres, which are several orders of magnitude more resolving than the synchrotron spatial scale, which is limited by the classical diffraction limit of a few µm. This can be seen from the comparison of the same 30 µm×30 µm region mapped by AFM-IR and with synchrotron IR micro-spectroscopy at the highest achievable spatial resolution (Fig. 3, lower panels; Yabuta et al. 2022; Mathurin et al. 2022a). The AFM-IR images show that phyllosilicates are widespread down to the finest scale (i.e. a few tens of nanometres). By contrast, isolated carbonates are visible and mixed into the phyllosilicates. The AFM-IR technique reveals the sizes of these phases below the synchrotron IR micro-spectroscopy diffraction limit. As an example, the large carbonate (about 10 µm large) that one can guess in the top right of the synchrotron IR micro-spectroscopy image (Fig. 3, bottom right), is clearly resolved and visible in the AFM-IR image (Fig. 3, bottom left). By contrast, the opaque phase detected in the centre of the synchrotron IR micro-spectroscopy image is also visible in the AFM-IR image but with contours somehow blurred, indicating that this opaque phase is most probably buried below the surface of the particle.

3.3. Composition of the Ryugu samples from infrared spectra

To present a chemical composition of the Ryugu samples, we derived the global spectrum for each sample, combining the respective MIR and FIR spectra (Fig. 5). Each spectrum was shifted by an arbitrary amount for clarity. In the upper right panel of Fig. 5, the spectra of saponite and serpentine are plotted for comparison (see Table A.1 and Glotch et al. 2007). In the top right of the figure, the reference spectra of three carbonates are shown: dolomite and magnesite ($CaMg(CO_3)_2$) and ($MgCO_3$), see Table A.1 and Roush 2021), and breunnerite ($Mg_{0.78}Fe_{0.22}CO_3$, this work). Figure 11 displays a close-up of selected spectra in the 1900–100 cm^{-1} spectral region, with reference spectra of possible mineral components. When the fraction of carbonates is high enough, the set of bands observed points to the identification of dolomite, as shown by

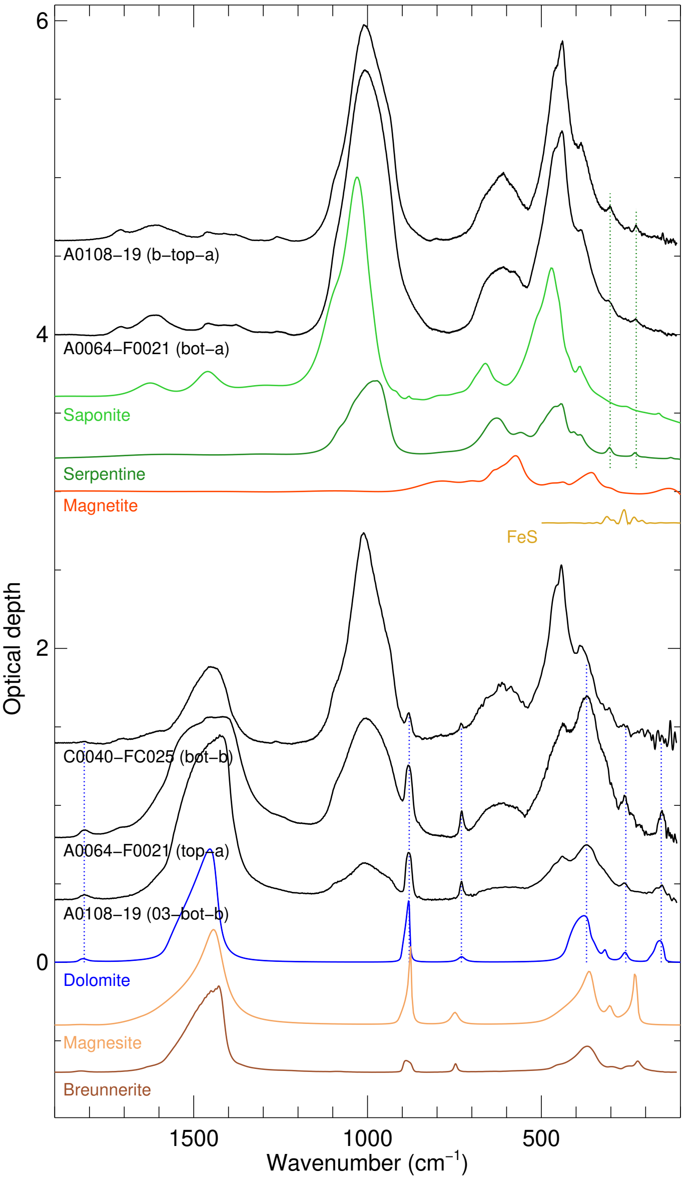

Fig. 11. Close-up of selected characteristic spectra of the Ryugu samples in the 1900–100 cm^{-1} range, with pure mineral spectra shown for reference (dolomite and magnesite, Roush 2021; breunnerite $Mg_{0.78}Fe_{0.22}CO_3$, this work; FeS Henning & Mutschke 1997; magnetite, Glotch & Rossman 2009; saponite and serpentine, Glotch et al. 2007). In the upper part of the figure, vertical dashed dark-green lines have been added to highlight the positions of specific small features of serpentine. In the lower part of the figure, vertical dashed blue lines are guides to the eye to show the characteristic positions of IR features in dolomite, which is the main carbonate identified in this work (see text for details).

the vertical dashed blue lines, with some bands in the FIR, such as at 160 cm^{-1}, which are very characteristic. Dolomite is the dominant carbonate found in this set of samples, at the scale of the synchrotron IR microscopy. On the phyllosilicate side, the spectra represent a main component of saponite mixed with serpentine that gives rise to a shoulder on the red wing of the SiO stretching mode absorption. In order to determine the respective contributions of the components present in each sample, each global spectrum was deconvolved into individual components, as shown in Fig. 2. The absorption bands of the so-called opaque minerals (magnetite and iron sulphides) are responsible for a significant part of the extinction of the IR continuum in some spectra, as shown in Fig. 1. Their contributions are hard to retrieve from the IR spectra in Fig. 11, because their vibrational mode absorption bands occurring in the FIR (e.g. around ~570 and ~360 cm^{-1} for magnetite, and around ~270 cm^{-1} for FeS, Glotch & Rossman 2009; Querry 1985; Mukai 1990; Henning & Mutschke 1997) are accompanied by a high refractive index, and the expected resulting low-contrast bands overlap with the intense bands of the other major mineral components present.

The OH-CH stretch region is decomposed in two global components. The CH stretching mode contribution was obtained by subtracting a local baseline continuum. The OH contribution was then measured by integrating over the CH subtracted spectrum. In the 1800–1280 cm^{-1} region, the spectrum was deconvolved using five Gaussians: one for the carbonyl (C=O) contribution peaking at about 1710 cm^{-1}, one for an OH bending peaking around 1640–1620 cm^{-1}, one for an aromatic C=C peaking around 1600 cm^{-1}, and two for bands peaking at 1500–1420 cm^{-1}, defining the carbonates' contribution. The silicates' contribution was obtained by integrating the spectrum in the 1200–800 cm^{-1} range, after subtracting the potential O–C–O out-of-plane mode of the carbonates. In the case where physisorbed and interlayer water represents an important contribution to the spectrum, the deconvolution of the C=C from the overlapping OH bending and aromatic C=C bands becomes challenging. In such a case, an estimate of the contribution of the OH bending mode can be evaluated from the measured OH stretching-mode integrated optical depth, applying a known intensity factor of 0.072, as discussed above. We thus estimated the C=C contribution either by direct deconvolution or by subtracting the expected OH bending contribution. If the OH integrated optical depth contribution represented a high fraction, more than half of the OH + C=C value, the evaluated aromatic C=C contribution was considered only as an upper limit. The column densities were then evaluated using the band strength previously discussed, and are reported in Table B.1 and presented in Fig. 9.

3.4. CH_2/CH_3 ratios

Close-ups of the absorption in the aliphatics region of the analysed samples are shown in Fig. 6. The methylene-to-methyl ratio of the aliphatic component is evaluated in two usual ways for comparison to other planetary samples. One commonly found indicator in the literature is the peak intensity maximum of the asymmetric stretching modes $I^{\rm peak}_{\rm CH_2}/I^{\rm peak}_{\rm CH_3}$. This indicator is straightforward and does not require a deconvolution of the individual contributing bands. To gain insight into the column density ratio of the methylene-to-methyl ratio, a deconvolution of the aliphatics band is more informative. Such a deconvolution is applied in the analysis of interstellar dust grains made of hydrogenated amorphous carbon (e.g. Dartois et al. 2004, 2007, and references therein). A minimum of five bands contribute to the aliphatic signature: the asymmetric CH_3 peaking around 2960 cm^{-1}, the asymmetric CH_2 peaking around 2920 cm^{-1}, a contribution from resonances of this last mode with overtones of the deformation modes, giving rise to an additional contribution in the 2900 cm^{-1} region, called the shoulder or Fermi resonance (this shoulder or resonance can be seen in the reference aliphatic spectra in the upper left of Fig. 6), the symmetric CH_3 peaking around 2880 cm^{-1}, and the symmetric CH_2 peaking around 2860 cm^{-1}. The spectra were deconvolved using five Gaussians assuming a common full width at half maximum for each band, and constraining the asymmetric to symmetric methyl band area to be 0.2, as measured in reference spectra (Dartois et al. 2004). This parametrisation, based on physico-chemistry constraints, avoids having to deal with too many free parameters that otherwise lead to a poor convergence of the fitting. The resulting fits are shown in Fig. 6, in red for methyl bands, and in blue for methylene bands. The overall fitted band is overlaid in cyan on the samples spectra. Care must be taken, in some cases, with the contribution of carbonate combination and overtone modes to this spectral region, when carbonates are abundant in the measured sample region of interest. This is shown for one sample in Fig. 6, where the contribution from dolomite to the spectrum is shown in brown, and the resulting dolomite-subtracted spectrum is shown just above. Once this deconvolution was performed, we integrated the asymmetric bands optical depth $\int \tau_{\rm CH_2} d\bar{\nu}$ and $\int \tau_{\rm CH_3} d\bar{\nu}$ and, using the integrated absorption coefficients of each mode, we derived the methylene-to-methyl column density ratios given in Table 2. As peak intensity ratios are commonly used in the literature, both peak ratios and column density ratios are displayed in Fig. 7 as a function of the CH to Si column density ratio. The methylene-to-methyl ratio expressed in column density spans the 3–5.5 range. The methylene-to-methyl column density ratios seems to show a slight correlation: the more abundant the CH, the higher the CH_2/CH_3 ratio seems to be. In the samples analysed, the ones with the lowest CH/Si abundance are from chamber C. These samples seem also to be related to the ones showing more aromatic C=C contributions. The interstellar medium (ISM) value for the $N(CH_2)/N(CH_3)$ ratio of hydrogenated amorphous carbons observed in the diffuse interstellar medium (DISM) is lower, around about 2–2.5 (e.g. Dartois et al. 2007; Sandford et al. 1991), or around 1–1.2 in peak intensity ratios. Figure 8 shows the comparison of CH_2/CH_3 peak ratios with literature data. The CH_2/CH_3 peak ratios in Ryugu are higher than the one typically observed for petrologic type 1 chondrites, and are comparable to the range observed for type 2 and 3 chondrites (Alexander et al. 2014; Briani et al. 2013; Dionnet et al. 2018; Kebukawa et al. 2010, 2011, 2019; Kerraouch et al. 2022; Merouane et al. 2012; Orthous-Daunay 2011, 2013; Quirico et al. 2018; Yesiltas et al. 2014, 2015, 2022; Yesiltas & Kebukawa 2016). This does not necessarily imply a higher level of heating of Ryugu than in C1 type chondrites, and should be constrained by other petrologic estimates. The Alexander et al. (2014) analysis of four lithologies in Tagish Lake IOM that have undergone different degrees of aqueous alteration suggest a negative correlation between the ratio of CH_2/CH_3 stretching bands with the (CH_2+CH_3)/C=C ratio, the least altered phase having the lowest CH_2/CH_3 ratio associated with the highest H/C ratio among the lithologies studied. The parent body aqueous alteration would, in this case, increase the CH_2/CH_3 ratio, but at the expense of H consumption as the carbon yield for the different lithologies varies much less. On the other hand, a recent report on the experimental aqueous alteration of the IOM of Paris at

Table 2. Aliphatic CH_2/CH_3 asymmetric vibrations' peak intensity ratios, asymmetric modes' integrated band ratios, and column density ratios.

Sample	$\frac{I^{\rm peak}_{\rm CH_2}}{I^{\rm peak}_{\rm CH_3}}$	$\frac{\int \tau_{\rm CH_2} {\rm d}\bar{\nu}}{\int \tau_{\rm CH_3} {\rm d}\bar{\nu}}$	$\frac{N_{\rm CH_2}}{N_{\rm CH_3}}$
A0064−FO013 (17-top-a)	1.97	2.87 ± 0.26	4.31 ± 0.40
A0108−15 (03-bot-a)	1.69	2.38 ± 0.27	3.57 ± 0.41
A0108−15 (03-bot-b)	1.98	2.74 ± 0.31	4.12 ± 0.46
A0108−15 (03-top-a)	1.83	2.70 ± 0.51	4.05 ± 0.76
A0108−19 (03-bot-a)	1.68	2.51 ± 0.46	3.77 ± 0.69
A0108−19 (b-bot-a)	1.80	2.62 ± 0.24	3.93 ± 0.36
A0108−19 (b-bot-b)	1.95	2.92 ± 0.38	4.37 ± 0.58
A0108−19 (b-top-a)	1.88	2.54 ± 0.47	3.81 ± 0.70
A0108−19 (b-top-b)	1.83	2.48 ± 0.39	3.72 ± 0.59
A0108−19 (b-top-c)	1.95	2.92 ± 0.38	4.37 ± 0.58
A0064−F0020 (bot-a)	1.99	2.67 ± 0.43	4.01 ± 0.65
A0064−F0020 (top-a)	2.06	2.90 ± 0.60	4.35 ± 0.90
A0064−F0021 (bot-a)	1.74	2.55 ± 0.20	3.82 ± 0.30
A0106−13 (bot-a)	1.73	2.43 ± 0.38	3.65 ± 0.56
A0106−13 (top-a)	1.98	2.94 ± 0.43	4.42 ± 0.64
A0106−13 (top-b)	2.01	2.86 ± 0.22	4.29 ± 0.33
C0046−FO004 (10-bot-a)	2.27	3.25 ± 0.82	4.87 ± 1.23
C0046−FO004 (10-top-1)	2.17	3.58 ± 0.49	5.37 ± 0.74
C0046−FO004 (10-top-2)	2.53	3.67 ± 0.35	5.51 ± 0.53
C0002−FC016 (bot-a)	2.10	2.94 ± 0.41	4.41 ± 0.62
C0002−FC016 (top-a)	2.16	2.95 ± 0.45	4.43 ± 0.67
C0040−FC025 (bot-a)	1.35	2.08 ± 0.13	3.11 ± 0.19
C0040−FC025 (bot-b)	1.48	2.19 ± 0.08	3.28 ± 0.12
C0109−4 (bot-a)	1.61	2.44 ± 0.36	3.65 ± 0.54
C0109−4 (top-a)	1.68	2.55 ± 0.43	3.83 ± 0.65
C0109−10 (bot-a)	2.00	3.52 ± 0.49	5.28 ± 0.73
C0109−10 (top-a)	1.77	2.82 ± 0.27	4.23 ± 0.41
C0057−5 (bot-a)	2.02	3.27 ± 0.76	4.90 ± 1.14
C0057−5 (bot-b)	1.84	2.58 ± 0.25	3.88 ± 0.38
C0057−5 (bot-c)	2.19	3.04 ± 0.20	4.56 ± 0.30
C0057−5 (bot-d)	1.83	3.24 ± 0.87	4.85 ± 1.30

Notes. The two spectra with a high fraction of dolomite contribution overlap are not included.

150°C, seems to show a decrease in the CH_2/CH_3 ratio upon aqueous alteration (Laurent et al. 2022). If the same view is applied to Ryugu, then the initial organic matter H/C should have been even higher before aqueous alteration than that observed today. Possible interactions between the organic phase during aqueous alteration of the Ryugu matrix should be investigated in more detail. The high CH_2/CH_3 ratio in Ryugu might also arise from intrinsic initial formation processes of the organic phase, which favoured a high CH_2/CH_3 ratio, meaning longer chains than usual when compared to unheated carbonaceous chondrites.

3.5. Abundances

A summary of the column densities of the identified IR functional groups is given in Table B.1. Relative proportions of the different groups (aliphatics, hydroxyl + interlayer and/or physisorbed water, carbonyl, carbonates, and silicates) from FTIR analysis of the different samples, shown per group (CH, OH, C=O, CO_3, and Si) are graphically presented in Fig. 9. The C=C contribution is not represented in the figure, as in many cases only upper limits could be calculated from the deconvolution due to the overlap with the OH bending mode in the samples (see below). Independent measurements of the Ryugu samples showed the presence of polycyclic aromatic hydrocarbons (PAHs) at the level of a few tens of nmol g^{-1} (a few ppm) during the extraction of soluble organic matter (Naraoka et al. 2022; Aponte et al. 2022). Thus, a possible contribution of aromatic C-H in the FTIR spectra at 3050 cm^{-1} at that abundance level is expected to be low.

The IR hyper-spectral maps show that Ryugu is dominated by phyllosilicates, with no identification of anhydrous silicate in our samples (Figs. 5 and 11). CI chondrites contain up to 94% phyllosilicates (Alfing et al. 2019; King et al. 2015), which are Fe-bearing Mg-rich serpentine and saponite (Tomeoka & Buseck 1988; Zolensky et al. 1993; Kerridge 1976; Osawa et al. 2005), except for Flensburg, which does not contain saponite (Bischoff et al. 2021). In Orgueil, the (most abundant) fine-grained phyllosilicates are usually mixed with fine ferrihydrite particles, whereas coarser phyllosilicates are devoid of ferrihydrite (Tomeoka & Buseck 1988). Ivuna, however, like the Ryugu samples, does not show the presence of ferrihydrite (Zolensky et al. 1993; Nakamura et al. 2023). Infrared spectra of CI chondrites show a sharp absorption at 3685 cm^{-1}, which is attributed to the presence of serpentine (Osawa et al. 2005; Takir et al. 2013). This feature is also observed in the Ryugu spectra, supporting the important presence of serpentine in the analysed samples, but saponite is also present in the Ryugu samples (see Fig. 11). Yokoyama et al. (2023) suggest a serpentine-to-saponite molar ratio of 3:2 in the Ryugu samples, which is compatible with our analyses (see Figs. 5 and 11). In CI chondrites, there are variations in the composition of phyllosilicates, with Mg# (defined as the atomic ratio 100 × Mg/(Mg+Fe)) varying from ~50 to ~85 (Kerridge 1976; Zolensky et al. 1993; Bischoff et al. 2021). Such heterogeneity in compositions could also explain the variations in the phyllosilicate features in the IR spectra of Ryugu. Carbonates in the Ryugu samples are dominated by dolomite, as is the case for CI chondrites (Johnson & Prinz 1993; Endress & Bischoff 1996). We see no evidence for other types of carbonates in our analyses, although rare occurrences of breunnerite and calcite have been reported in Ryugu by other studies (Yokoyama et al. 2023; Nakamura et al. 2023). In CI chondrites, the abundance of carbonates is around 0.5–3 vol%, the abundance of magnetite varies from 5–10 vol%, and pyrrhotite (the main Fe sulphide) is present at the level of a few percent (Alfing et al. 2019; King et al. 2015). In the Ryugu crushed samples, we can sometimes optically identify the framboidal magnetite, but from the Ryugu hyper-spectral maps it is difficult to quantify the abundance of magnetite or pyrrhotite, as they have a very high refractive index. Nevertheless, it can be observed that the total projected surface of the opaques' ROIs (as shown, for instance, in the bottom panels of Figs. 4 or C.1) is always a few times higher than that of the carbonates in the vast majority of the hyper-spectral maps, except for the samples in which a large single carbonate is measured. Using the IR column densities (N) reported in Table B.1 (and represented in Fig. 9), the volume ratio of carbonates to phyllosilicates can be evaluated. We assumed a density of $\rho_{\rm dolomite} \sim 2.8$ g cm^{-3} for a molar mass of $M_{\rm dolomite}$ ~184 g mol^{-1} (it should be noted that $n_{\rm CO_3} = 2$ as there are two CO_3 groups for one Ca atom in dolomite). For phyllosilicates we assumed the Glotch et al. (2007) formula for saponite and serpentine (Table A.1), with molar masses of $M_{\rm Saponite}$ ~376 g mol^{-1} and $M_{\rm Serpentine}$ ~281 g mol^{-1}, and for Si atoms, we assumed $n_{\rm Si} = 3.96$ and $n_{\rm Si} = 1.8$ in each formula, respectively. We assumed densities of $\rho_{\rm saponite} \sim 2.3$ g cm^{-3} and

$\rho_{\mathrm{serpentine}} \sim 2.6\ \mathrm{g\,cm^{-3}}$, respectively. Assuming an average 3:2 serpentine-to-saponite ratio (Yokoyama et al. 2023), we can calculate:

$$f = \frac{\mathrm{volume}_{\mathrm{carbonates}}}{\mathrm{volume}_{\mathrm{phyllosilicates}}}, \tag{9}$$

$$f = \frac{N_{\mathrm{CO_3}}}{N_{\mathrm{Si}}} \frac{M_{\mathrm{dolomite}/n_{\mathrm{CO_3}}}}{\rho_{\mathrm{dolomite}}} \left\langle \frac{\rho_{\mathrm{phyllosilicates}}}{M_{\mathrm{phyllosilicates}/n_{\mathrm{Si}}}} \right\rangle, \tag{10}$$

where

$$M_{\mathrm{dolomite}/n_{\mathrm{CO_3}}} = \frac{M_{\mathrm{dolomite}}}{n_{\mathrm{CO_3}}} = \frac{M_{\mathrm{dolomite}}}{2}, \tag{11}$$

and

$$\left\langle \frac{M_{\mathrm{phyllosilicates}/n_{\mathrm{Si}}}}{\rho_{\mathrm{phyllosilicates}}} \right\rangle = \frac{3}{5}\frac{M_{\mathrm{serpentine}}}{\rho_{\mathrm{serpentine}}}/1.8 + \frac{2}{5}\frac{M_{\mathrm{saponite}}}{\rho_{\mathrm{saponite}}}/3.96, \tag{12}$$

and then

$$\mathrm{Volume}\left(\frac{\mathrm{carbonates}}{\mathrm{phyllosilicates + carbonates}}\right) = (1 + 1/\mathrm{f})^{-1}. \tag{13}$$

In the Ryugu samples, the average relative volume of carbonates to phyllosilicate and carbonates using Eq. (13) is shown in Fig. 10. Error bars were calculated assuming the extreme cases of pure serpentine or pure saponite composition for the phyllosilicates. The volume ratios for most Ryugu data are at the high end of the range of volume ratios in CI chondrites reported in Alfing et al. (2019) and King et al. (2015). In a few cases, the volume ratios are very high because these samples contain large, single carbonates. It is important to note that the IR spectra are sensitive to the whole volume probed (column density), and thus the numbers are slightly different from the volume ratios estimated from the polished sections. The volume fractions of dolomite were reported as 1.8% and 2.9% in plates 5 and 6, respectively, of the C0002 samples, by Nakamura et al. (2023). These values translate to 2.1% and 3.2% when recalculated using Eq. (13), and these are plotted as red dots in Fig. 10.

The mean C/Si abundance ratio by weight for CI chondrites is 3.48 wt%/10.7 wt% (e.g. Palme et al. 2014; Lodders et al. 2009; Anders & Grevesse 1989), corresponding to a C/Si atomic ratio of about 0.76. For Ryugu the mean value measured for C is 4.63 wt%, with 3.08 wt% attributed to organic carbon (Yurimoto et al. 2022; Yokoyama et al. 2023), and thus the Ryugu organic fraction is in line with CI values. The CH to Si abundance we measured varies from 0.5 to 1.5 among the different samples measured (Table B.1). With the CH_2/CH_3 ratio measured (Fig. 7), it corresponds to an aliphatic C/Si atomic ratio of about half of this number, that is to say an atomic $C^{\mathrm{aliphatics}}/Si$ ratio in the 0.25–0.75 range in our samples.

The mean carbonyl-to-CH ratio retrieved from the deconvolution is in the 0.013–0.064 range, with a mean around 0.034 ± 0.032 (2σ). The lowest values can, however, be slightly underestimated in the deconvolution if the OH bending mode contribution in the wing of the band is significant. Given the measured CH_2/CH_3 ratio of about two (Fig. 7), the $C{=}O/CH_x$ ratio (i.e. per CH_x group) would be about twice the C=O/CH ratio, in the range 0.029–0.14. Previous nuclear magnetic resonance studies (Cody & Alexander 2005; Derenne & Robert 2010) measured a $C{=}O/CH_x$ ratio for Orgueil that is higher than this range, suggesting that the Ryugu samples could contain more CH than Orgueil. To confirm this statement, it would be interesting to compare the $C{=}O/CH_x$ ratio of Orgueil and Ryugu IOM residues using the same deconvolution.

As stated before, the backbone on which these aliphatics are attached also comprises aromatic carbons, which are observed also via Raman spectroscopy D and G bands (e.g. Bonal et al. 2022), and are widespread, as are the CH aliphatics in the IR measurements. Abundance with Raman is not easily accessible as this is emission spectroscopy and also because these C=C modes can be resonant. In the IR measurements, this aromatic C=C band contribution is accessible, although it is still less straightforward to derive in the whole-rock spectra as it can be overlapped with strong inter-layer bending modes from physisorbed water and saponite bands, possibly contributing to the spectra. We thus decided to calculate this contribution only as an upper limit to the aromatic C=C contribution, which is close to the true C=C column density for the spectra where these OH bending and/or saponite contributions are the least intense. This aromatic C column density is of the same order as the aliphatic C one. Some Ryugu fragments measured depart from the mean, such as the C0109 sample (see, lower spectrum of Fig. 2), for which the aromatic carbon contribution after spectral decomposition, as observed around 1600 $\mathrm{cm^{-1}}$, is higher. For these samples, the aromatic carbon column density is larger than the aliphatic carbon one, and thus has more polyaromatic moieties. The carbonate contribution is highly variable at the scale probed, and in a few samples we observed very large individual carbonate grains. In the measured samples, except for the carbonate grain we focused specifically on, the carbonate CO_3 group variations observed with respect to the aliphatic carbon give an atomic $C^{\mathrm{carbonates}}/C^{\mathrm{aliphatics}}$ ratio in the 0.03–0.34 range, with a median of 0.14 ± 0.08 (1σ). The size distribution histogram of carbonates extracted from the maps show no particular behaviour. The biggest carbonates have large sizes of several thousands of square micrometres in projected size, and are isolated from a continuum of much smaller carbonates. The biggest one we measured (A0108-19 sample) is largely dominated by a dolomite composition from the positions of the bands in the FIR.

4. Summary and outlooks

Several Ryugu grains from chambers A and C were analysed by synchrotron IR micro-spectroscopy at the diffraction limit (~6 × 6 µm), providing hyper-spectral maps that record the spatial distributions of the main bands of organics, carbonates, and phyllosilicates. Strong absorption of the IR continuum also revealed the presence of minerals with a high refractive index in the samples, such as magnetite and Fe sulphides. Additional measurements allowed us to extend the wavelength range to the FIR at the scales of the grains studied, providing better assignments for the carbonates' and phyllosilicates' composition. The Ryugu IR spectra are compatible with CI chondrites spectra, with the silicates dominated by phyllosilicates. We did not identify any anhydrous silicates in the samples analysed. The carbonates are dominated by dolomite, as also observed in CI chondrites. The hyper-spectral maps show that the aliphatics organics are distributed all over the samples, and intimately mixed with the phyllosilicates at the scale of a few microns probed by the synchrotron beam. The methylene-to-methyl (CH_2/CH_3) column density ratio of the analysed samples varies between about 3.5 and five (or between about 1.5–2.5 in peak intensity ratio), which is compatible with what is typically observed in IOM from carbonaceous chondrites (Quirico et al. 2018; Kebukawa et al. 2011), and higher than the value determined in the DISM (Dartois et al. 2007; Sandford et al. 1991). The possible correlation observed between the CH_2/CH_3 ratio and the CH/Si ratio (Fig. 7) suggests a possible mixing of several organic phases, with an organic phase more ramified or with shorter chains associated with the phyllosilicates, and slightly longer chains, and therefore a CH_2-richer phase, when the organics' abundance is higher locally.

Acknowledgements. This work was carried out in the frame of the Hayabusa2 Initial Analysis Teams, in the IOM sub-team led by Prof. H. Yabuta and the Stone sub-team led by Prof. T. Nakamura. Spectral data will be available on the Data ARchives and Transmission System (DARTS) of the Japan Aerospace Exploration Agency (JAXA). Part of the equipment used in this work has been financed by the French INSU-CNRS program "Physique et Chimie du Milieu Interstellaire" (PCMI). This work was supported in France by the Centre National d'Etudes Spatiales (CNES) for the participation to analyses of samples returned by the Hayabusa2 mission. We acknowledge synchrotron SOLEIL for provision of synchrotron radiation facilities for access to the SMIS beamline. We thank Sylvie Heron for providing us the n-tetracosane reference sample. We are grateful to Timothy D. Glotch for his constructive comments and recommendations.

References

Alexander, C. M. O., Fogel, M., Yabuta, H., & Cody, G. D. 2007, Geochim. Cosmochim. Acta, 71, 4380

Alexander, C. O., Cody, G., Kebukawa, Y., et al. 2014, Meteor. Planet. Sci., 49, 503

Alfing, J., Patzek, M., & Bischoff, A. 2019, Geochemistry, 79, 125532

Anders, E., & Grevesse, N. 1989, Geochim. Cosmochim. Acta, 53, 197

Anthony, J. W., Bideaux, R. A., Bladh, K. W., & Nichols, M. C. 2001, Handbook of Mineralogy, 1 (Mineral Data Publ.)

Aponte, J. C., Dworkin, J., Glavin, D., et al. 2022, Earth, Planets and Space, submitted

Bertie, J. E., & Lan, Z. 1996, Appl. Spectrosc., 50, 1047

Bischoff, A., Alexander, C. M. O., Barrat, J.-A., et al. 2021, Geochim. Cosmochim. Acta, 293, 142

Bonal, L., Quirico, E., Montagnac, G., et al. 2022, in 53rd Lunar and Planetary Science Conference, 2678, LPI Contributions, 1331

Briani, G., Quirico, E., Gounelle, M., et al. 2013, Geoch. Cosmochim. Acta, 122, 267

Cody, G. D., & Alexander, C. M. O. D. 2005, Geochim. Cosmochim. Acta, 69, 1085

Dartois, E., Muñoz Caro, G. M., Deboffle, D., & d'Hendecourt, L. 2004, A&A, 423, L33

Dartois, E., Geballe, T. R., Pino, T., et al. 2007, A&A, 463, 635

Dartois, E., Engrand, C., Brunetto, R., et al. 2013, Icarus, 224, 243

Dazzi, A., & Prater, C. B. 2017, Chem. Rev., 117, 5146

Dazzi, A., Prazeres, R., Glotin, F., & Ortega, J. 2005, Opt. Lett., 30, 2388

Derenne, S., & Robert, F. 2010, Meteor. Planet. Sci., 45, 1461

Dionnet, Z., Aléon-Toppani, A., Borondics, F., et al. 2018, Microsc. Microanal., 24, 2100

Endress, M., & Bischoff, A. 1996, GCA, 60, 489

Flynn, G. J., Keller, L. P., Feser, M., Wirick, S., & Jacobsen, C. 2003, Geochim. Cosmochim. Acta, 67, 4791

Glotch, T. D., & Rossman, G. R. 2009, Icarus, 204, 663

Glotch, T. D., Rossman, G. R., & Aharonson, O. 2007, Icarus, 192, 605

Godard, M., Geballe, T. R., Dartois, E., & Muñoz Caro, G. M. 2012, A&A, 537, A27

Henning, T., & Mutschke, H. 1997, A&A, 327, 743

Jiang, C.-L., Zeng, W., Liu, F.-S., Tang, B., & Liu, Q.-J. 2019, J. Phys. Chem. Solids, 131, 1

Johnson, C. A., & Prinz, M. 1993, Geochim. Cosmochim. Acta, 57, 2843

Kebukawa, Y., Alexander, C. M. O. D., & Cody, G. D. 2011, Geochim. Cosmochim. Acta, 75, 3530

Kebukawa, Y., Nakashima, S., Ishikawa, M., et al. 2010, Meteor. Planet. Sci., 45, 394

Kebukawa, Y., Alexander, C. M. O., & Cody, G. D. 2019, Meteor. Planet. Sci., 54, 1632

Keller, L. P., Bajt, S., Baratta, G. A., et al. 2006, Science, 314, 1728

Kerraouch, I., Kebukawa, Y., Bischoff, A., et al. 2022, Geochim. Cosmochim. Acta, 334, 155

Kerridge, J. F. 1976, Earth Planet. Sci. Lett., 29, 194

King, A., Schofield, P., Howard, K., & Russell, S. 2015, Geochim. Cosmochim. Acta, 165, 148

Kloprogge, J. T., & Ponce, C. P. 2021, Minerals, 11, 112

Laurent, B., Holin, M., Bernard, S., et al. 2022, in 53rd Lunar and Planetary Science Conference, 2678, LPI Contributions, 1432

Lodders, K., Palme, H., & Gail, H. P. 2009, Landolt-Börnstein (Springer-Verlag Berlin Heidelberg), 4B, 712

Mathurin, J., Dartois, E., Pino, T., et al. 2019, A&A, 622, A160

Mathurin, J., Deniset-Besseau, A., & Dazzi, A. 2020, Acta Phys. Polon. A, 137, 29

Mathurin, J., Dartois, E., Dazzi, A., et al. 2022a, in 53rd Lunar and Planetary Science Conference, 2678, LPI Contributions, 2142

Mathurin, J., Deniset-Besseau, A., Bazin, D., et al. 2022b, J. Appl. Phys., 131, 010901

Merouane, S., Djouadi, Z., d'Hendecourt, L. L. S., Zanda, B., & Borg, J. 2012, ApJ, 756, 154

Mooney, T., & Knacke, R. F. 1985, Icarus, 64, 493

Mukai, T. 1990, Evolution of Interstellar Dust and Related Topics, 397

Nakamura, T., Matsumoto, M., Amano, K., et al. 2023, Science in press, `https://doi.org/10.1126/science.abn8671`

Naraoka, H., Takano, Y., Dworkin, J. P., et al. 2022, Science, submitted

Orthous-Daunay, F.-R. 2011, Ph.D. thesis, Université de Grenoble, France

Orthous-Daunay, F. R., Quirico, E., Beck, P., et al. 2013, Icarus, 223, 534

Osawa, T., Kagi, H., Nakamura, T., & Noguchi, T. 2005, Meteor. Planet. Sci., 40, 71

Palme, H., Lodders, K., & Jones, A. 2014, in Planets, Asteriods, Comets and The Solar System, 2, ed. A. M. Davis, 15

Pendleton, Y., Sandford, S., Allamandola, L., Tielens, A., & Sellgren, K. 1994, ApJ, 437, 683

Phan, V. T. H., Quirico, E., Beck, P., et al. 2021, Spectrochim. Acta A: Mol. Spectrosc., 259, 119853

Querry, M. R. 1985, Optical constants, Tech. rep. (Missouri Univ-Kansas City)

Quirico, E., Bonal, L., Beck, P., et al. 2018, Geochim. Cosmochim. Acta, 241, 17

Roush, T. L. 2021, Icarus, 354, 114056

Roush, T., Pollack, J., & Orenberg, J. 1991, Icarus, 94, 191

Sandford, S., Allamandola, L., Tielens, A., et al. 1991, ApJ, 371, 607

Sawada, H., Okazaki, R., Tachibana, S., et al. 2017, Space Sci. Rev., 208, 81

Tachibana, S., Abe, M., Arakawa, M., et al. 2014, Geochem. J., 48, 571

Tachibana, S., Sawada, H., Okazaki, R., et al. 2022, Science, 375, 1011

Takir, D., Emery, J. P., Mcsween Jr., H. Y., et al. 2013, Meteor. Planet. Sci., 48, 1618

Tomeoka, K., & Buseck, P. R. 1988, GCA, 52, 1627

Tsuda, Y., Saiki, T., Terui, F., et al. 2020, Acta Astronaut., 171, 42

Yabuta, H., Cody, C. D., Engrand, C., et al. 2022, Science, submitted

Yesiltas, M., & Kebukawa, Y. 2016, Meteor. Planet. Sci., 51, 584

Yesiltas, M., Kebukawa, Y., Peale, R. E., et al. 2014, Meteor. Planet. Sci., 49, 2027

Yesiltas, M., Peale, R. E., Unger, M., Sedlmair, J., & Hirschmugl, C. J. 2015, Meteor. Planet. Sci., 50, 1684

Yesiltas, M., Kebukawa, Y., Glotch, T. D., et al. 2022, Meteor. Planet. Sci., 57, 1665

Yokoyama, T., Nagashima, K., Nakai, I., et al. 2023, Science, in press, `https://doi.org/10.1126/science.abn7850`

Yurimoto, H., Hayabusa2-Initial-Analysis Chemistry Team, & Hayabusa2-Initial-Analysis Core 2022, in 53rd Lunar and Planetary Science Conference, 2678, LPI Contributions, 1377

Zolensky, M., Barrett, R., & Browning, L. 1993, Geochim. Cosmochim. Acta, 57, 3123

---

[1] Institut des Sciences Moléculaires d'Orsay, CNRS, Univ. Paris-Saclay, 91405 Orsay, France
e-mail: `emmanuel.dartois@universite-paris-saclay.fr`

[2] Faculty of Engineering, Yokohama National University, Yokohama, Kanagawa, 240-8501, Japan

[3] Department of Earth and Planetary Systems Science, Hiroshima University, Higashi-Hiroshima, Hiroshima 739-8526, Japan

[4] Institut Chimie Physique (ICP), UMR 8000, Université Paris-Saclay, CNRS, Orsay, 91405, France

[5] IJCLab, UMR 9012, Université Paris-Saclay, CNRS, 91405 Orsay, France

[6] Institut de Minéralogie, Physique des Matériaux et de Cosmochimie, Museum National d'Histoire Naturelle, CNRS, Sorbonne Université, Paris 75231, France

[7] Institut de Planétologie et d'Astrophysique, Université Grenoble Alpes, Grenoble 38000, France

[8] Synchrotron SOLEIL, CNRS, CEA, Paris-Saclay, France
[9] Earth and Planets Laboratory, Carnegie Institution of Washington, 5241 Broad Branch Road NW, Washington, DC 20015, USA
[10] Materials Science and Technology Division, US Naval Research Laboratory, Washington, DC 20375, USA
[11] Graduate School of Environmental Studies, Nagoya University, Chikusa-ku, Nagoya 464-8601, Japan
[12] Advanced Light Source, Lawrence Berkeley National Laboratory, Berkeley, CA 94720-8229, USA
[13] The Graduate University for Advanced Studies, SOKENDAI, Hayama, Kanagawa 240-0193, Japan
[14] Department of Earth Sciences, Waseda University, Shinjuku-ku, Tokyo 169-8050, Japan
[15] Centro de Química Estrutural, Institute of Molecular Sciences and Department of Chemical Engineering, Instituto Superior Técnico, Universidade de Lisboa, Av. Rovisco Pais 1, 1049-001 Lisboa, Portugal
[16] Department of Earth Sciences, Tohoku University, Sendai 980-8578, Japan
[17] École normale supérieure de Lyon, Université de Lyon, 69342 Lyon, France
[18] Institute for Molecular Science, UVSOR Synchrotron Facility, Myodaiji, Okazaki 444-8585, Japan
[19] Department of Earth and Planetary Science, The University of Tokyo, Bunkyo-ku, Tokyo 113-0033, Japan
[20] NASA Ames Research Center, Moffett Field, CA 94035-1000, USA
[21] Department of Earth and Planetary Systems Science, Hiroshima University, Higashi-Hiroshima, Hiroshima 739-8526, Japan
[22] Materials Science and Technology Division, US Naval Research Laboratory, Washington, DC 20375, USA
[23] Spectroscopy Division, Japan Synchrotron Radiation Research Institute (JASRI), Sayo-gun, Hyogo 679-5198, Japan
[24] Institute of Materials Structure Science, High Energy Accelerator Research Organization, KEK, Tsukuba, Ibaraki, 305-0801, Japan
[25] Research and Utilization Division, Japan Synchrotron Radiation Research Institute (JASRI), Sayo-gun, Hyogo 679-5198, Japan
[26] Division of Earth and Planetary Sciences, Kyoto University, Kitashirakawa Oiwakecho, Sakyo-ku, Kyoto 606-8502, Japan
[27] Department of Earth and Planetary Sciences, Kyushu University, Fukuoka 819-0395, Japan
[28] Institute of Space and Astronautical Science, Japan Aerospace Exploration Agency, Sagamihara 252-5210, Japan
[29] Department of Natural History Sciences, Hokkaido University, Sapporo 060-0810, Japan
[30] Isotope Imaging Laboratory, Creative Research Institution, Hokkaido University, Sapporo 001-0021, Japan
[31] Kanagawa Institute of Technology, Atsugi 243-0292, Japan
[32] Department of Earth and Planetary Sciences, Nagoya University, Nagoya 464-8601, Japan

Appendix A: Band strengths

Table A.1: Integrated absorption coefficients (band strengths) $\mathcal{A}$ (cm/[group]) of selected IR vibrations identified in the Ryugu samples, with their respective parameters and corresponding literature references.

Species / Mode	Label	$\bar{\nu}(<\bar{\nu}>)^a$ (cm^{-1})	Wavelength (μm)	$\mathcal{A}$ (cm/[group])^b	int. range (cm^{-1})	ref
Water						
OH stretch		3400	2.94	7.7×10^{-17}/ OH		11
OH bending		1640	6.10	5.5×10^{-18}/ OH		11
Organics						
CH_3 a-stretch		2960	3.38	1.2-1.25×10^{-17}/ CH_3		2,3
CH_2 a-stretch		2925	3.42	7.4-8.4×10^{-18}/ CH_2		2,3
CH_3 s-stretch		2876	3.48	2-2.1×10^{-18}/ CH_3		2,3
CH_2 s-stretch		2855	3.50	2.1-2.4×10^{-18}/ CH_2		2,3
Average aliphatic CH band		-	-	$\approx4.8\times10^{-18}$/ CH		2,3
C=O str. (ketone)		1710		2.2×10^{-17}/ C=O		3
Arom. C=C str. (IOM)		1600		$3.2\pm0.4\times10^{-18}$/ C		1
Arom. C=C str.		1600		3.04×10^{-18}/ C ^{c}		4
Arom. C=C str. (UCAMM)		1600		$1.5\pm0.5\times10^{-18}$/ C		5
Arom. C=C str. (PAH)		1600		1-2.5×10^{-19}/ C		2
Dolomite $CaMg(CO_3)_2$						
CO_3 a-stretch	ν27-28	1442 (1469.8)	6.93 (6.80)	1.81×10^{-16}/ CO_3	1700-1200	1,6,7
O-C-O out-of-plane def.	ν23	880 (884.6)	11.36 (11.30)	1.67×10^{-17}/ CO_3	940-820	1,6,7
O-C-O in-plane def.	ν21-22	730 (729 .1)	13.69 (13.72)	2.92×10^{-18}/ CO_3	780-680	1,6,7
Magnesite $Mg(CO_3)$						
CO_3 a-stretch	ν27-28	1444 (1467)	6.92 (6.82)	2.35×10^{-16}/ CO_3	1700-1200	1,6,7
O-C-O out-of-plane def.	ν23	876 (882.3)	11.42(11.33)	2.71×10^{-17}/ CO_3	940-820	1,6,7
O-C-O in-plane def.	ν21-22	748 (747.9)	13.37 (13.37)	8.57×10^{-18}/ CO_3	800-690	1,6,7
Calcite $Ca(CO_3)$						
CO_3 a-stretch	ν27-28	1408 (1440.6)	7.10 (6.94)	2.46×10^{-16}/ CO_3	1700-1200	1,6,7
O-C-O out-of-plane def.	ν23	872 (875.6)	11.46(11.42)	1.74×10^{-17}/ CO_3	940-820	1,6,7
O-C-O in-plane def.	ν21-22	712 (711.7)	14.05 (14.05)	2.42×10^{-18}/ CO_3	750-670	1,6,7
Saponite $(Li_{0.09}Mg_{2.72}Fe^{3+}_{0.03}Al_{0.07})(Al_{0.04}Si_{3.96})O_{10}(OH)_2$						
SiO stretch		1030.1(1045.8)	9.71(9.56)	1.40×10^{-16}/Si	1250-850	1,8
Saponite $(Na_{0.22}Mg_{2.08}Fe^{3+}_{0.04}Al_{0.32}Si_{3.03})O_{10}(OH)_2$						
SiO stretch		1024.0(1037.1)	9.77(9.64)	1.17×10^{-16}/Si	1250-850	1,9
Serpentine $(Mg_{2.61}Fe_{0.31})(Si_{1.80}Al_{0.06})O_5(OH)_4$						
SiO stretch		980.0(1000.5)	10.20(9.99)	1.45×10^{-16}/Si	1250-850	1,8
Serpentine $(Mg_{2.75}Fe_{0.13})(Si_{1.85}Al_{0.07})O_5(OH)_4$						
SiO stretch		950.0(977.3)	10.53(10.23)	1.37×10^{-16}/Si	1250-850	1,10
Serpentine $(Mg_{2.81}Fe_{0.35})(Si_{1.87}Al_{0.07})O_5(OH)_4$						
SiO stretch		972.8(1010.2)	10.28(9.90)	1.62×10^{-16}/Si	1250-850	1,8

[a] The first number is the peak maximum position and the number in parenthesis is the average position in the reference samples. The average position is the one that would be observed at very low spectral resolution. The peak positions in the Ryugu samples are very close to the literature positions.
[b] The densities adopted to evaluate the integrated absorption cross sections for the minerals are: dolomite 2.86g/cm^3, magnesite 3.01g/cm^3, calcite 2.71g/cm^3 Anthony et al. (2001) [c] Assuming the relation $\mathcal{A}_{CH}/\mathcal{A}_{CC}$ = 1.578 given in Phan et al. (2021); [1] this work; [2] Dartois et al. (2007); [3] Dartois et al. (2004); [4] Phan et al. (2021); [5] Dartois et al. (2013); [6] Roush (2021); [7] Jiang et al. (2019); [8] Glotch et al. (2007); [9] Roush et al. (1991); [10] Mooney & Knacke (1985); [11] (Bertie & Lan 1996)

Appendix B: Chemical composition

Table B.1: Chemical composition of the Ryugu samples from FTIR

Sample	$\int \tau d\bar{\nu}$ [cm^{-1}]						Column density [10^{17}cm^{-2}]					
	OH (str.)	Aliphatics (CH str.)	Carbonyl (C=O str.)	Aro C=C (C=C str.)	Carbonates (CO_3 str.)	Silicates (SiO str.)	N(OH)	N(CH)	N(C=O)	N(Aro C=C)	N(CO_3)	N(Si)
						Chamber A						
A0064–*FO*013–17–*top*–*a*	22.44	2.95	0.43	≤ 0.33	5.08	61.09	2.24± 0.45	6.15± 1.23	0.20± 0.04	≤ 1.05	0.28± 0.06	4.36± 0.87
A0108–15–03–*bot*–*a*	43.18	2.20	0.18	≤ 5.74	7.55	76.38	4.32± 0.86	4.59± 0.92	0.08± 0.02	≤ 18.22	0.42± 0.08	5.46± 1.09
A0108–15–03–*bot*–*b*	69.68	2.33	0.14	≤ 4.29	6.22	84.21	6.97± 1.39	4.86± 0.97	0.06± 0.01	≤ 13.62	0.34± 0.07	6.01± 1.20
A0108–15–03–*top*–*a*	32.72	1.98	0.18	≤ 2.91	4.10	58.68	3.27± 0.65	4.12± 0.82	0.08± 0.02	≤ 9.24	0.23± 0.05	4.19± 0.84
A0108–19–03–*bot*–*a*	51.43	4.05	0.94	≤ 1.57	16.58	127.93	5.14± 1.03	8.43± 1.69	0.43± 0.09	≤ 4.97	0.92± 0.18	9.14± 1.83
A0108–19–03–*top*–*a*	19.52	2.04	0.40	≤ 1.62	5.54	65.44	1.95± 0.39	4.25± 0.85	0.18± 0.04	≤ 5.15	0.31± 0.06	4.67± 0.93
A0108–19*b*–*bot*–*a*	54.46	5.55	1.53	≤ 27.22	9.85	137.54	5.45± 1.09	11.55± 2.31	0.70± 0.14	≤ 86.42	0.54± 0.11	9.82± 1.96
A0108–19*b*–*bot*–*b*	14.42	2.06	0.82	≤ 2.22	3.11	57.01	1.44± 0.29	4.29± 0.86	0.37± 0.07	≤ 7.06	0.17± 0.03	4.07± 0.81
A0108–19*b*–*top*–*a*	72.16	8.33	2.11	≤ 1.99	99.34	188.23	7.22± 1.44	17.35± 3.47	0.96± 0.19	≤ 6.33	5.49± 1.10	13.44± 2.69
A0108–19*b*–*top*–*b*	51.23	7.83	2.37	≤ 7.45	6.83	146.13	5.12± 1.02	16.32± 3.26	1.08± 0.22	≤ 23.65	0.38± 0.08	10.44± 2.09
A0108–19*b*–*top*–*c*	14.40	2.06	0.82	≤ 1.99	3.21	56.97	1.44± 0.29	4.29± 0.86	0.37± 0.07	≤ 6.30	0.18± 0.04	4.07± 0.81
A0064–*F*0020–*bot*–*a*	52.98	6.99	1.78	≤ 2.70	1.65	166.49	5.30± 1.06	14.57± 2.91	0.81± 0.16	≤ 8.56	0.09± 0.02	11.89± 2.38
A0064–*F*0020–*top*–*a*	24.02	4.23	0.87	≤ 1.14	0.57	92.00	2.40± 0.48	8.80± 1.76	0.39± 0.08	≤ 3.62	0.03± 0.01	6.57± 1.31
A0064–*F*0021–*bot*–*a*	94.40	9.86	2.20	≤ 5.04	6.90	251.47	9.44± 1.89	20.54± 4.11	1.00± 0.20	≤ 15.99	0.38± 0.08	17.96± 3.59
A0064–*F*0021–*top*–*a*	32.04	6.02	0.31	≤ 0.08	135.01	111.70	3.20± 0.64	12.54± 2.51	0.14± 0.03	≤ 0.24	7.46± 1.49	7.98± 1.60
A0106–13–*bot*–*a*	75.28	5.92	1.43	≤ 8.28	12.95	169.08	7.53± 1.51	12.32± 2.46	0.65± 0.13	≤ 26.28	0.72± 0.14	12.08± 2.42
A0106–13–*top*–*a*	44.74	5.08	0.95	≤ 1.21	4.55	109.83	4.47± 0.89	10.57± 2.11	0.43± 0.09	≤ 3.85	0.25± 0.05	7.84± 1.57
A0106–13–*top*–*b*	36.38	3.72	2.13	≤ 2.54	10.44	99.35	3.64± 0.73	7.75± 1.55	0.97± 0.19	≤ 8.06	0.58± 0.12	7.10± 1.42
						Chamber C						
C0046–*FO*004–010–*bot*–*a*	38.72	4.73	0.58	≤ 2.88	3.98	106.21	3.87± 0.77	9.85± 1.97	0.27± 0.05	≤ 9.15	0.22± 0.04	7.59± 1.52
C0046–*FO*004–010–*top*1	38.67	4.31	0.43	≤ 2.53	10.22	83.20	3.87± 0.77	8.97± 1.79	0.19± 0.04	≤ 8.02	0.56± 0.11	5.94± 1.19
C0046–*FO*004–010–*top*2	34.11	2.46	0.45	≤ 1.98	1.50	66.77	3.41± 0.68	5.12± 1.02	0.20± 0.04	≤ 6.28	0.08± 0.02	4.77± 0.95
C0002–*FC*016–*bot*–*a*	20.35	2.31	0.31	≤ 1.07	2.53	60.04	2.04± 0.41	4.82± 0.96	0.14± 0.03	≤ 3.39	0.14± 0.03	4.29± 0.86
C0002–*FC*016–*top*–*a*	34.08	3.55	0.44	≤ 2.86	7.48	94.72	3.41± 0.68	7.40± 1.48	0.20± 0.04	≤ 9.09	0.41± 0.08	6.77± 1.35
C0040–*FC*025–*bot*–*a*	31.79	2.50	0.72	≤ 1.51	7.01	130.20	3.18± 0.64	5.20± 1.04	0.33± 0.07	≤ 4.80	0.39± 0.08	9.30± 1.86
C0040–*FC*025–*bot*–*b*	34.85	3.76	0.79	≤ 3.59	63.91	158.20	3.49± 0.70	7.83± 1.57	0.36± 0.07	≤ 11.39	3.53± 0.71	11.30± 2.26
C0109–04–*bot*–*a*	37.14	1.93	1.06	≤ 10.55	3.56	95.71	3.71± 0.74	4.02± 0.80	0.48± 0.10	≤ 33.51	0.20± 0.04	6.84± 1.37
C0109–04–*top*–*a*	30.49	1.60	0.33	≤ 8.63	2.97	82.88	3.05± 0.61	3.33± 0.67	0.15± 0.03	≤ 27.40	0.16± 0.03	5.92± 1.18
C0109–10–*bot*–*a*	25.32	2.27	0.17	≤ 5.22	2.90	86.39	2.53± 0.51	4.73± 0.95	0.08± 0.02	≤ 16.58	0.16± 0.03	6.17± 1.23
C0109–10–*top*–*a*	74.23	5.09	1.26	≤ 11.15	13.97	207.36	7.42± 1.48	10.60± 2.12	0.57± 0.11	≤ 35.39	0.77± 0.15	14.81± 2.96
C0057–5–*bot*–*a*	14.91	0.80	0.48	≤ 1.07	2.45	31.88	1.49± 0.30	1.67± 0.33	0.22± 0.04	≤ 3.41	0.14± 0.03	2.28± 0.46
C0057–5–*bot*–*c*	18.68	0.95	0.42	≤ 0.70	6.62	43.58	1.87± 0.37	1.98± 0.40	0.19± 0.04	≤ 2.23	0.37± 0.07	3.11± 0.62
C0057–5–*bot*–*d*	12.93	1.39	0.32	≤ 1.03	10.21	32.84	1.29± 0.26	2.90± 0.58	0.14± 0.03	≤ 3.26	0.56± 0.11	2.35± 0.47

[a] The integration is performed in energy units (wavenumber)

Appendix C: Synchrotron maps

Synchrotron maps of the various samples are displayed in each figure for: a (silicates, green), b (carbonates, red), c (opaques, yellow-orange), d (OH stretch, blue), e (CH stretch, magenta), and f (corresponding visible image).

C.1. Chamber A

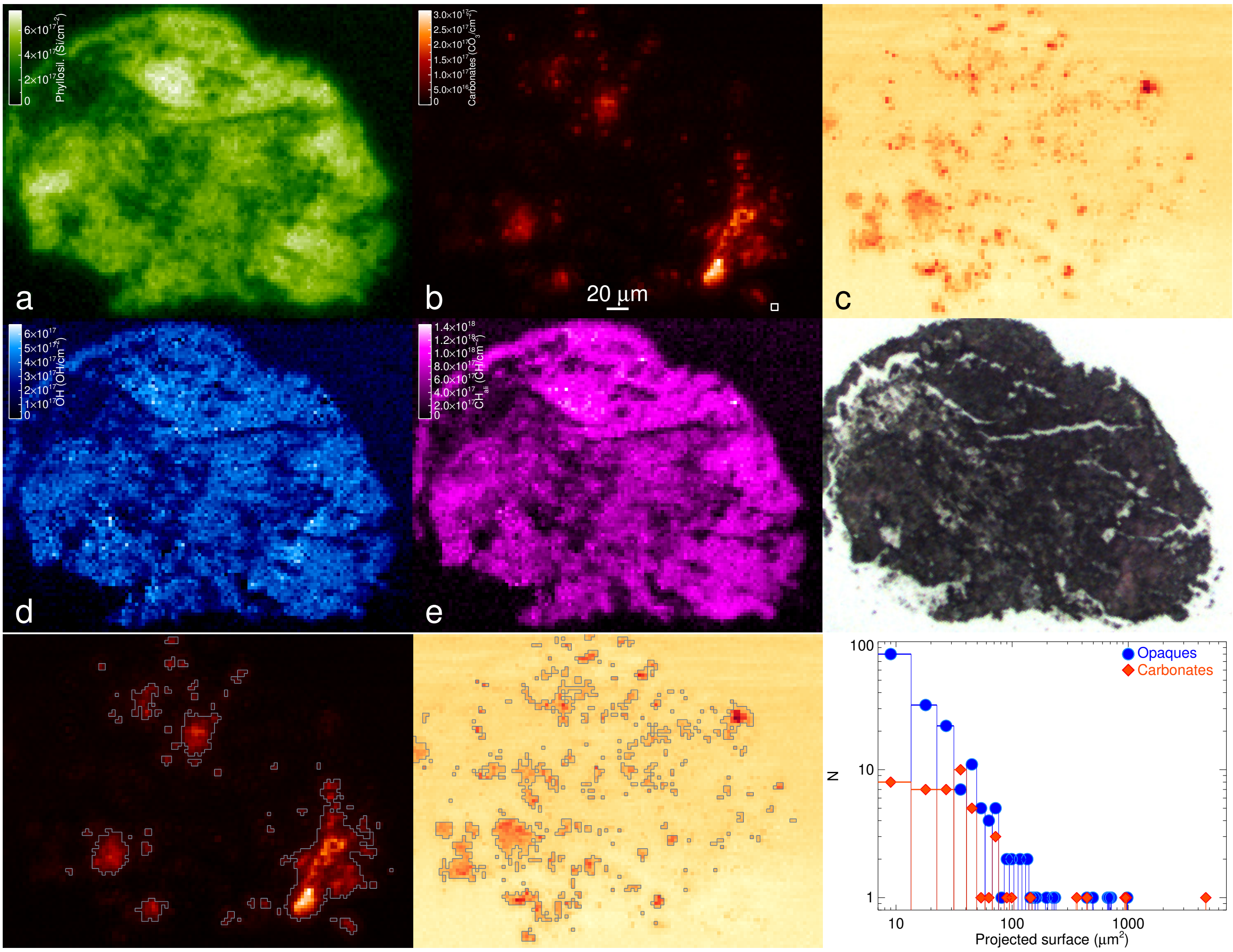

Fig. C.1: Chamber A: A0064-FO013-17-top, ROI size distributions determined in a similar way as explained in caption of Fig. 4.

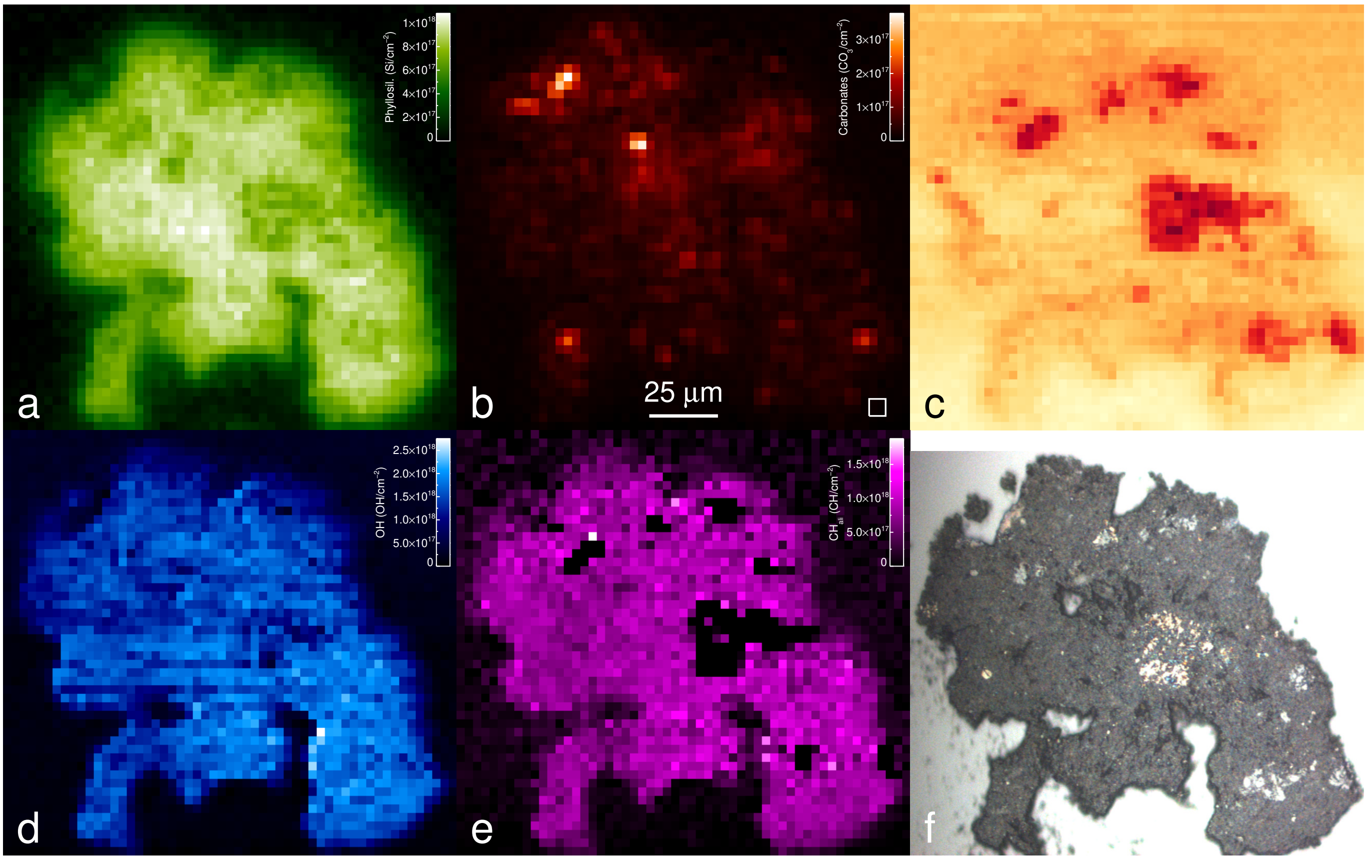

Fig. C.2: Chamber A: A0108-15-03-bot-a

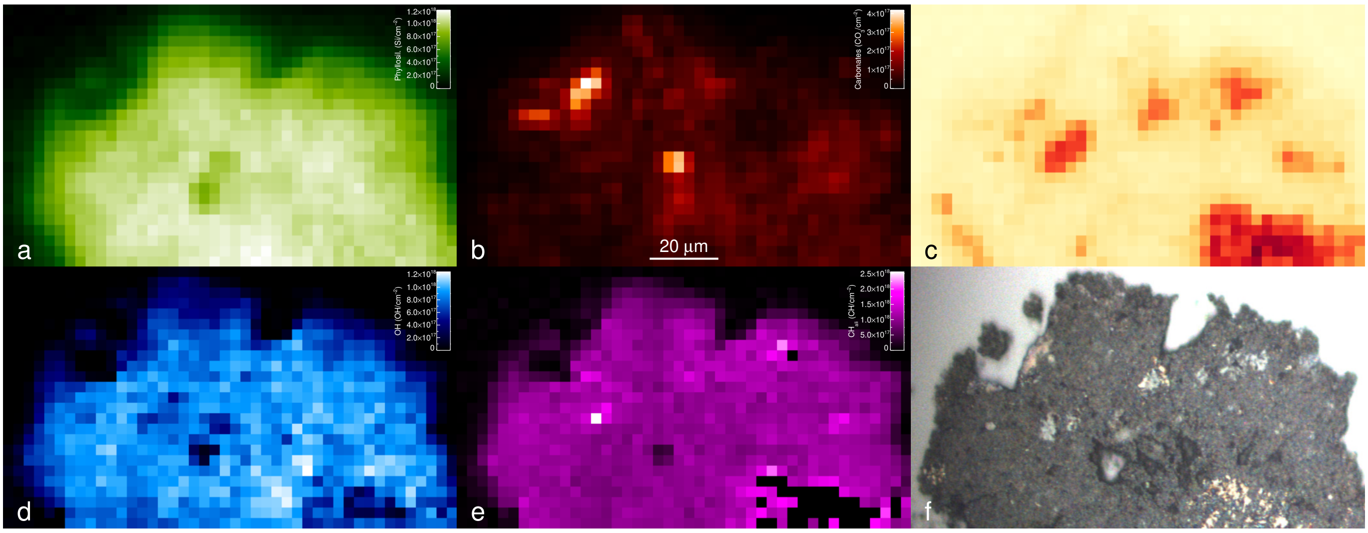

Fig. C.3: Chamber A: A0108-15-03-bot-b

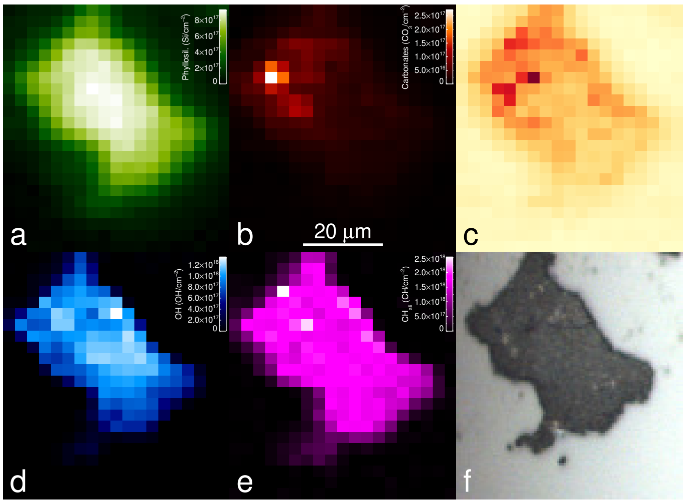

Fig. C.4: Chamber A: A0108-15-03 Bottom

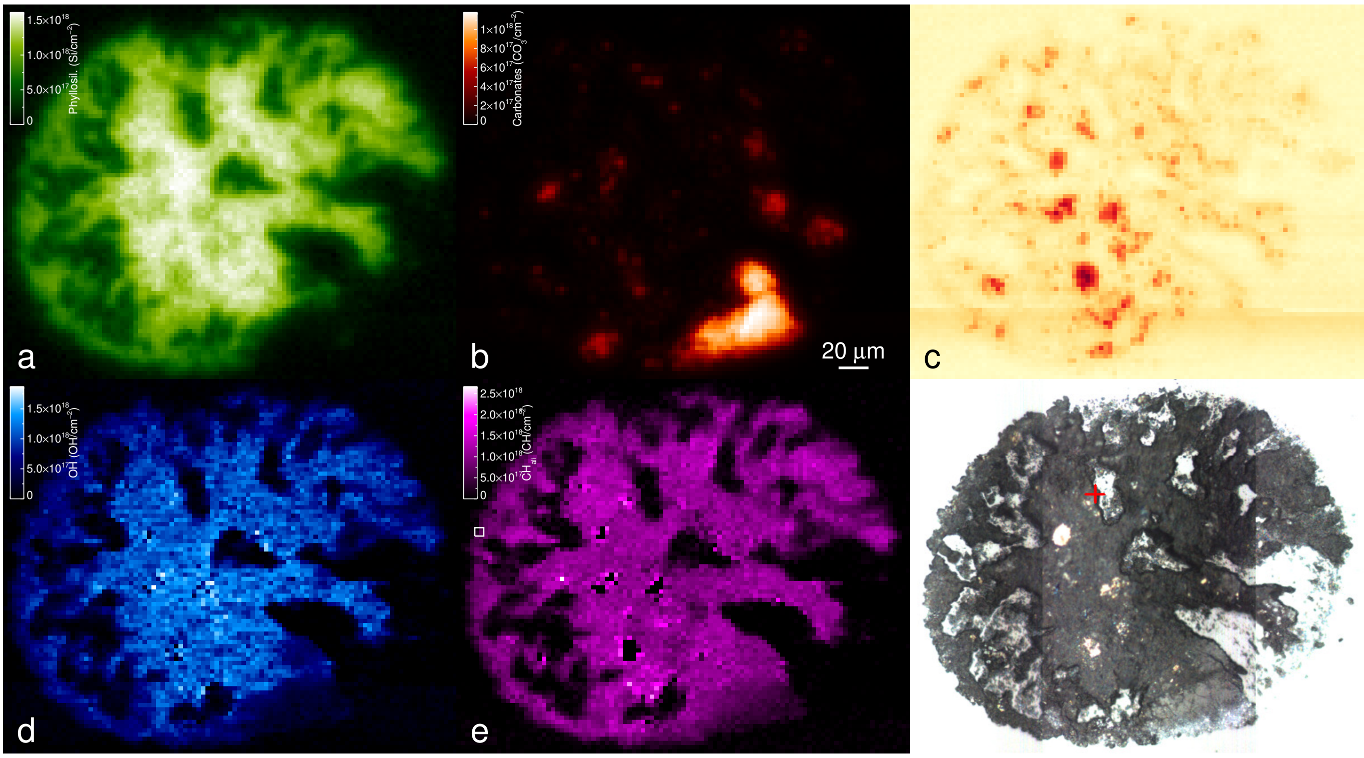

Fig. C.5: Chamber A: A0108-19-03-bot-a

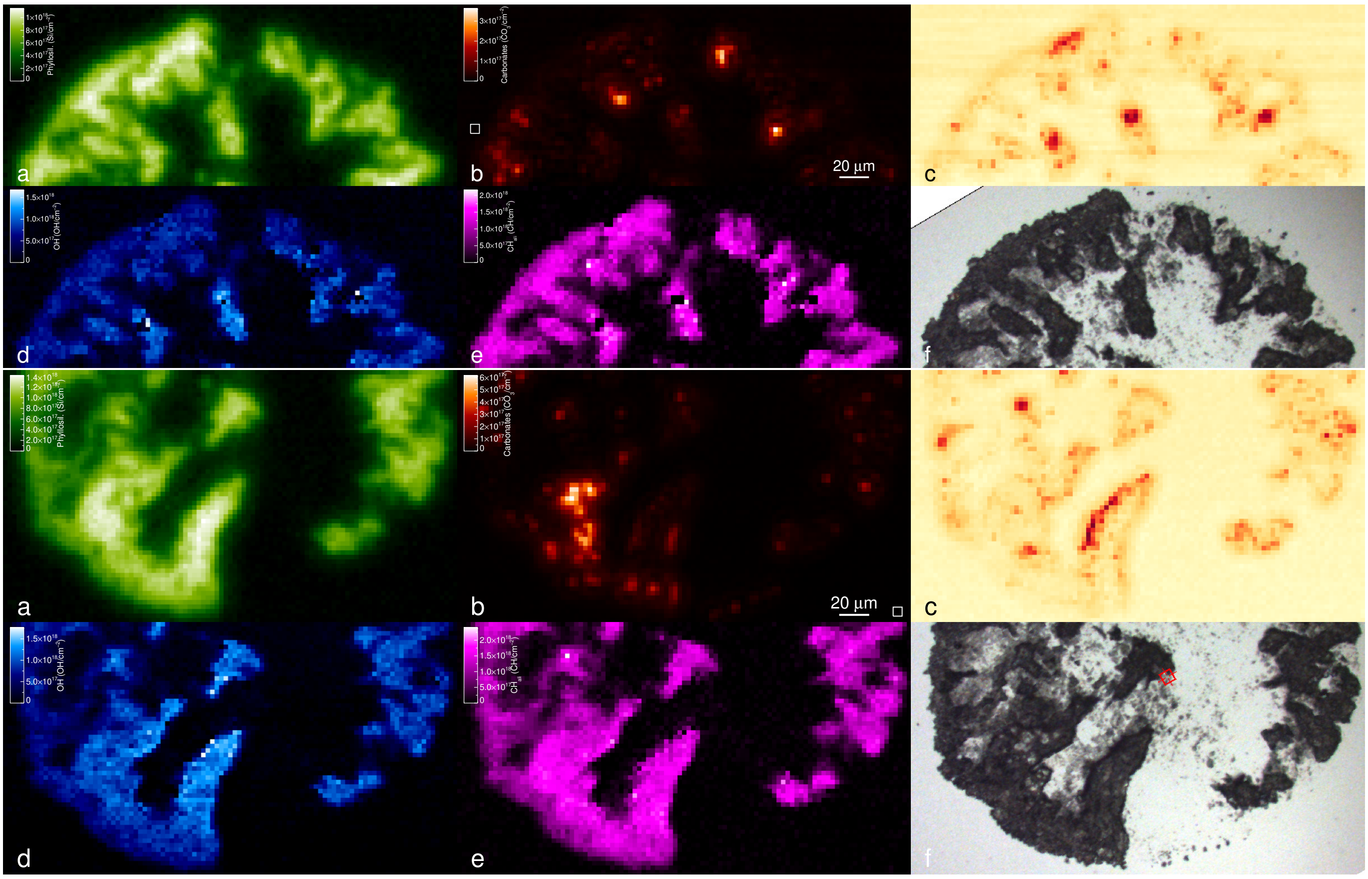

Fig. C.6: Chamber A: A0108-19-03-top-a

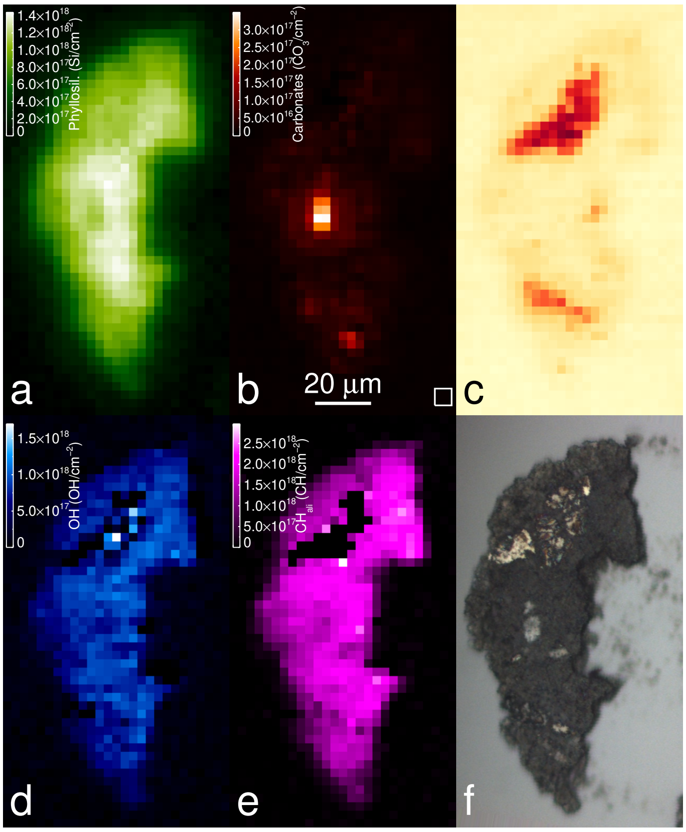

Fig. C.7: Chamber A: A0108-19b-bot-a

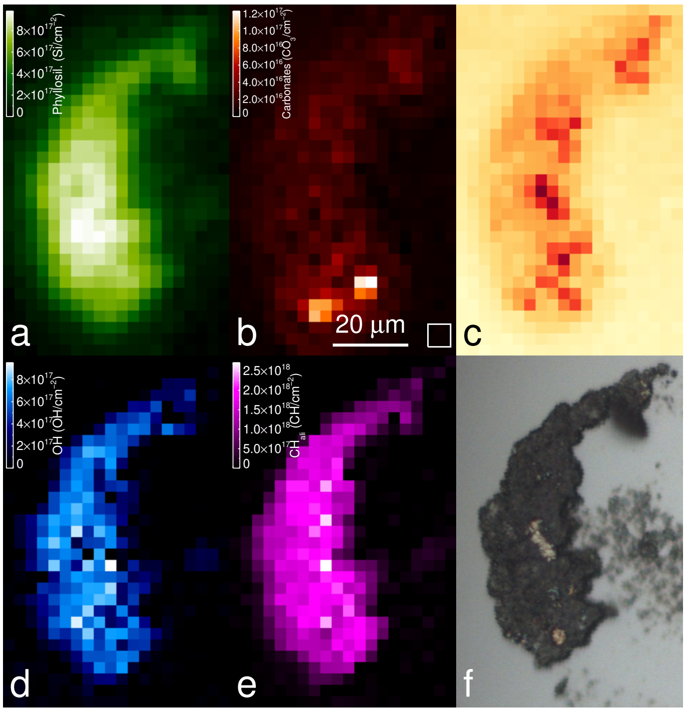

Fig. C.8: Chamber A: A0108-19b-bot-b

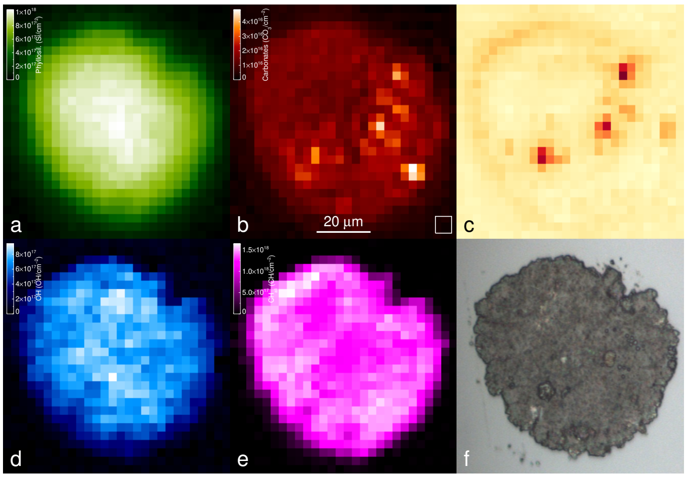

Fig. C.9: Chamber A: A0108-19b-top-a

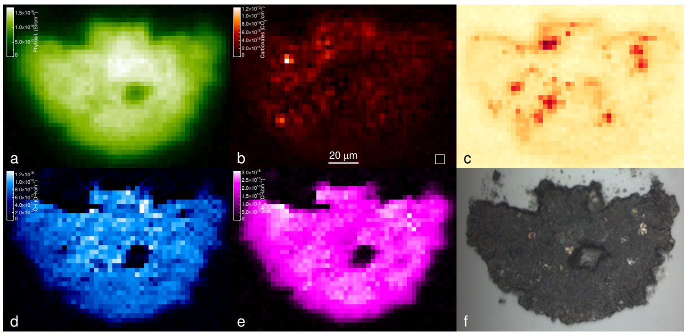

Fig. C.10: Chamber A: A0108-19b-top-b

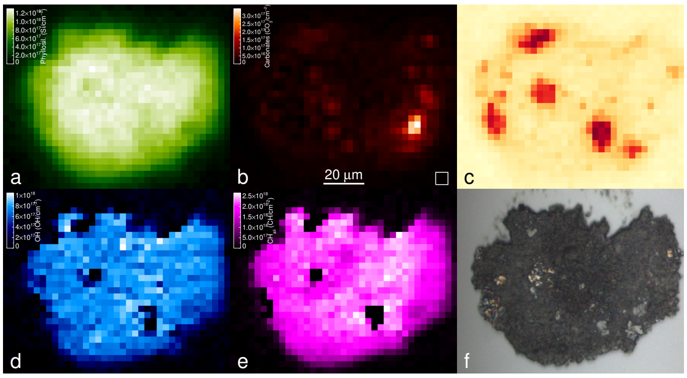

Fig. C.11: Chamber A: A0108-19b-top-c

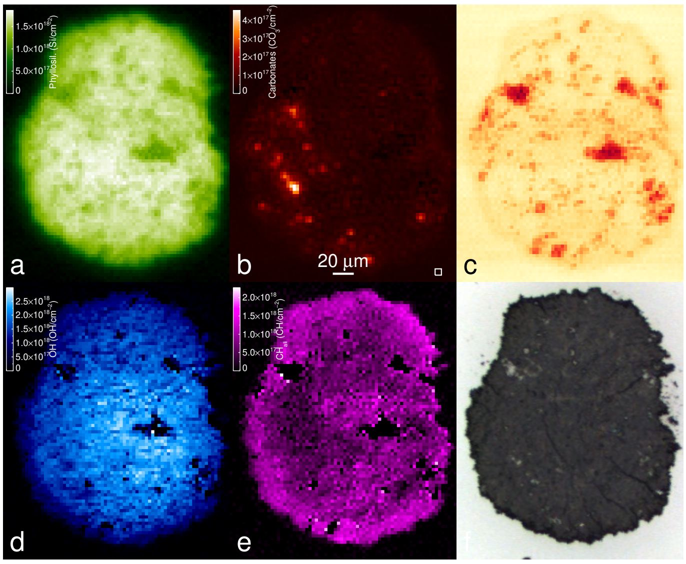

Fig. C.12: Chamber A: A0106-13-bot-a

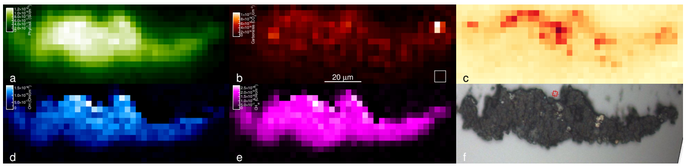

Fig. C.13: Chamber A: A0106-13-top-a

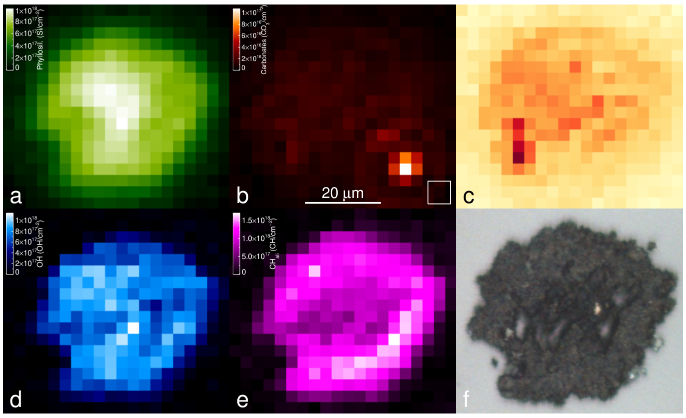

Fig. C.14: Chamber A: A0106-13-top-b

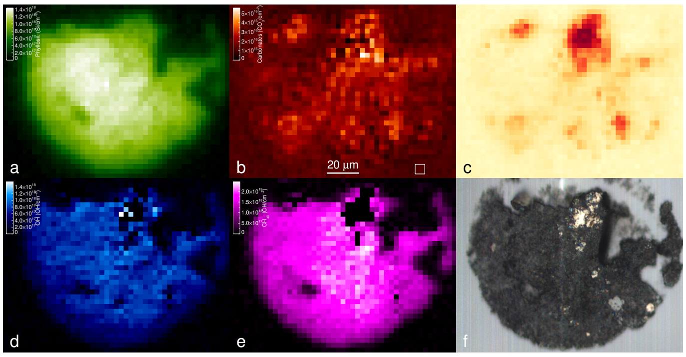

Fig. C.15: Chamber A: A0064-F0020-bot-a

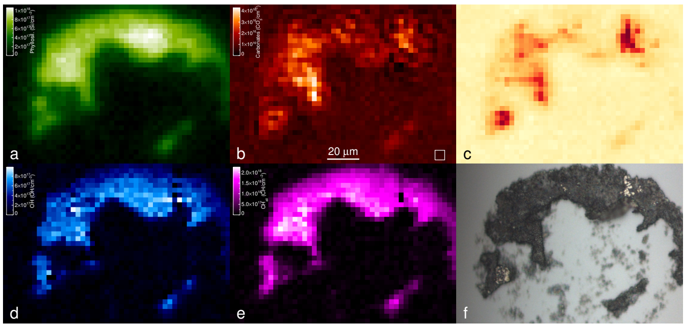

Fig. C.16: Chamber A: A0064-F0020-top-a

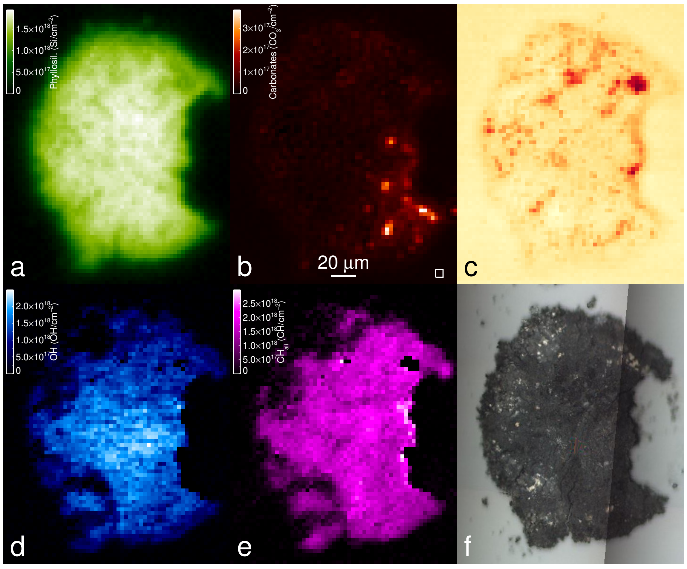

Fig. C.17: Chamber A: A0064-F0021-bot-a

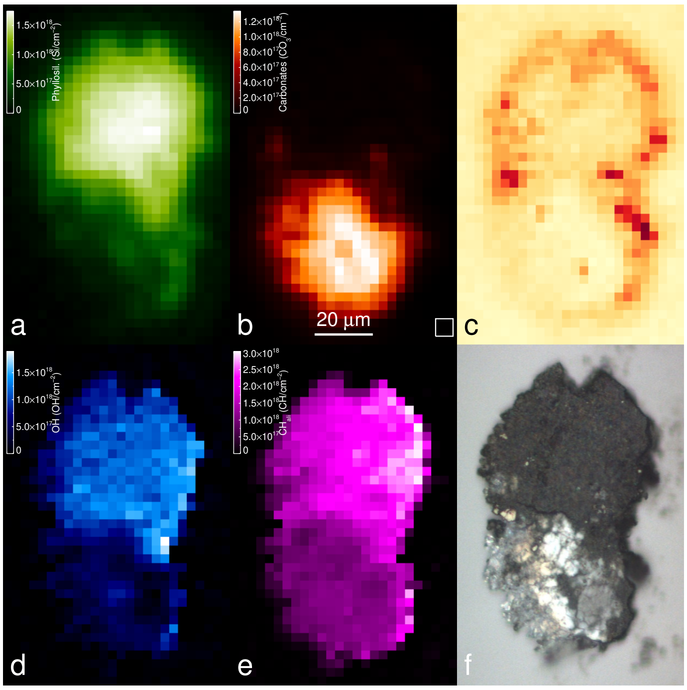

Fig. C.18: Chamber A: A0064-F0021-top-a

C.2. Chamber C

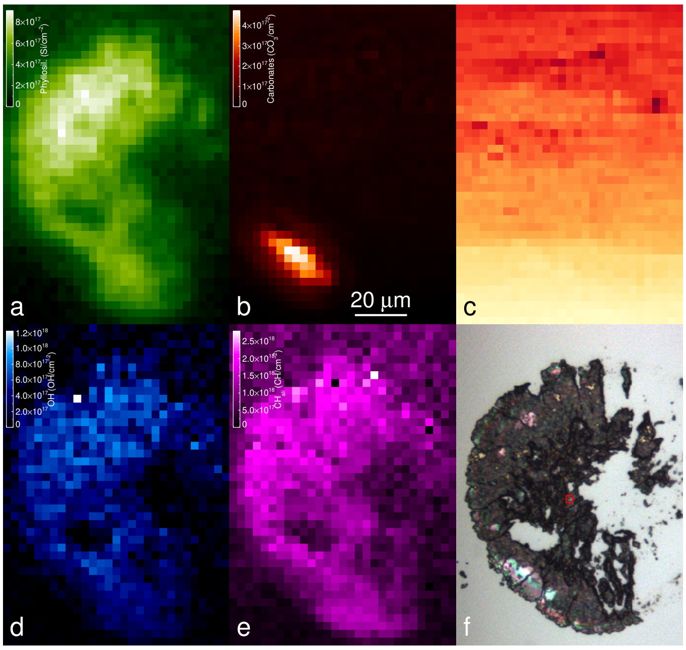

Fig. C.19: Chamber C: C0046-FO004-010-top1

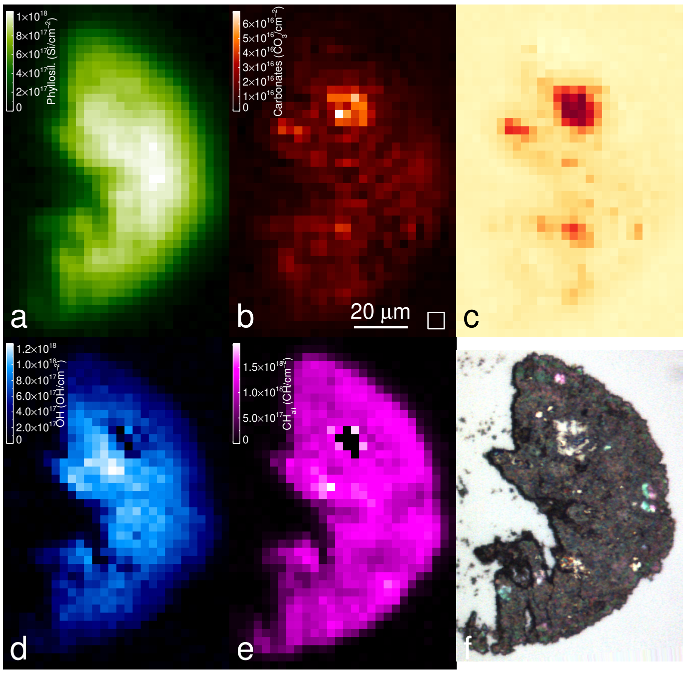

Fig. C.20: Chamber C: C0046-FO004-010-bot-a

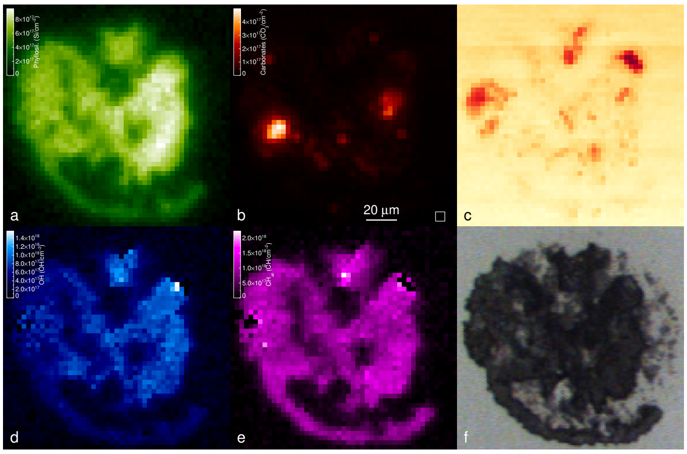

Fig. C.21: Chamber C: C0002-FC016-top-a

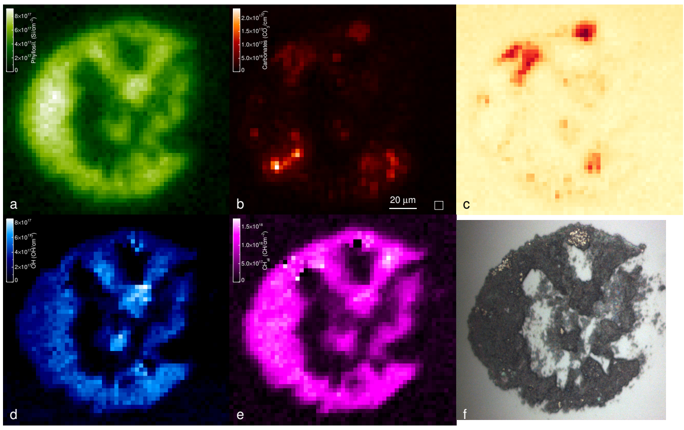

Fig. C.22: Chamber C: C0002-FC016-bot-a

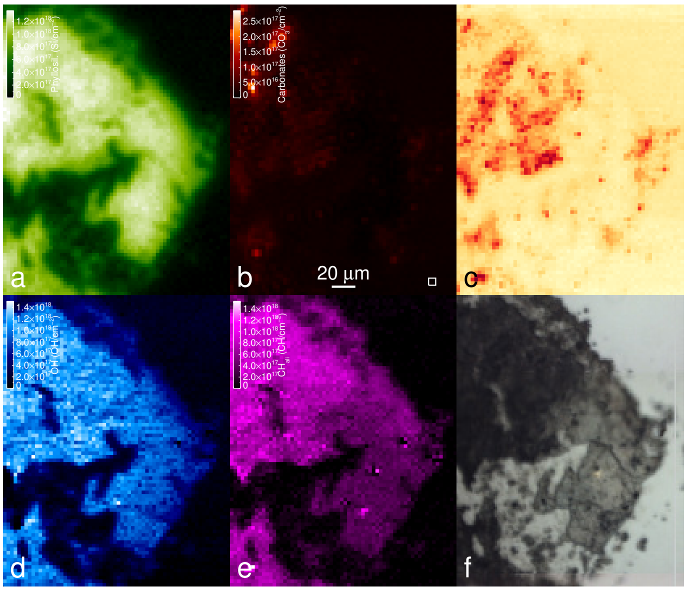

Fig. C.23: Chamber C: C0040-FC025-bot-a

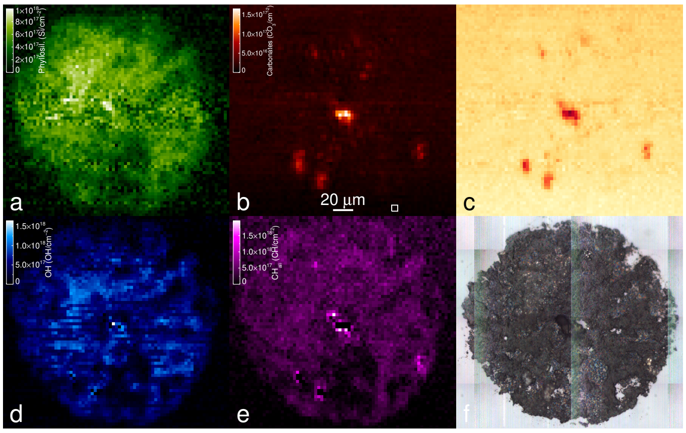

Fig. C.24: Chamber C: C0109-4-bot-a

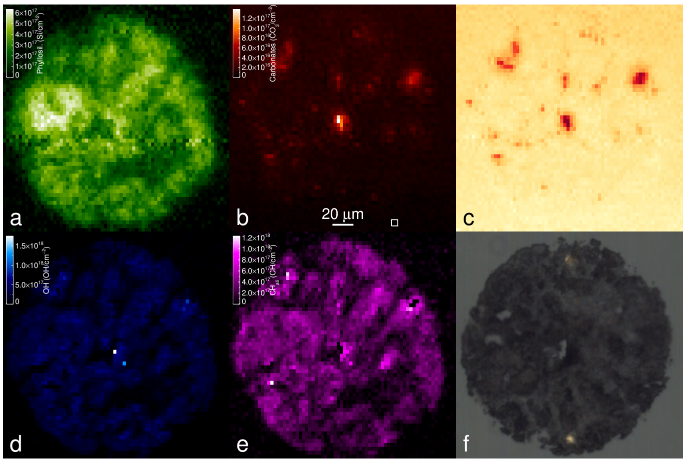

Fig. C.25: Chamber C: C0109-04-top-a

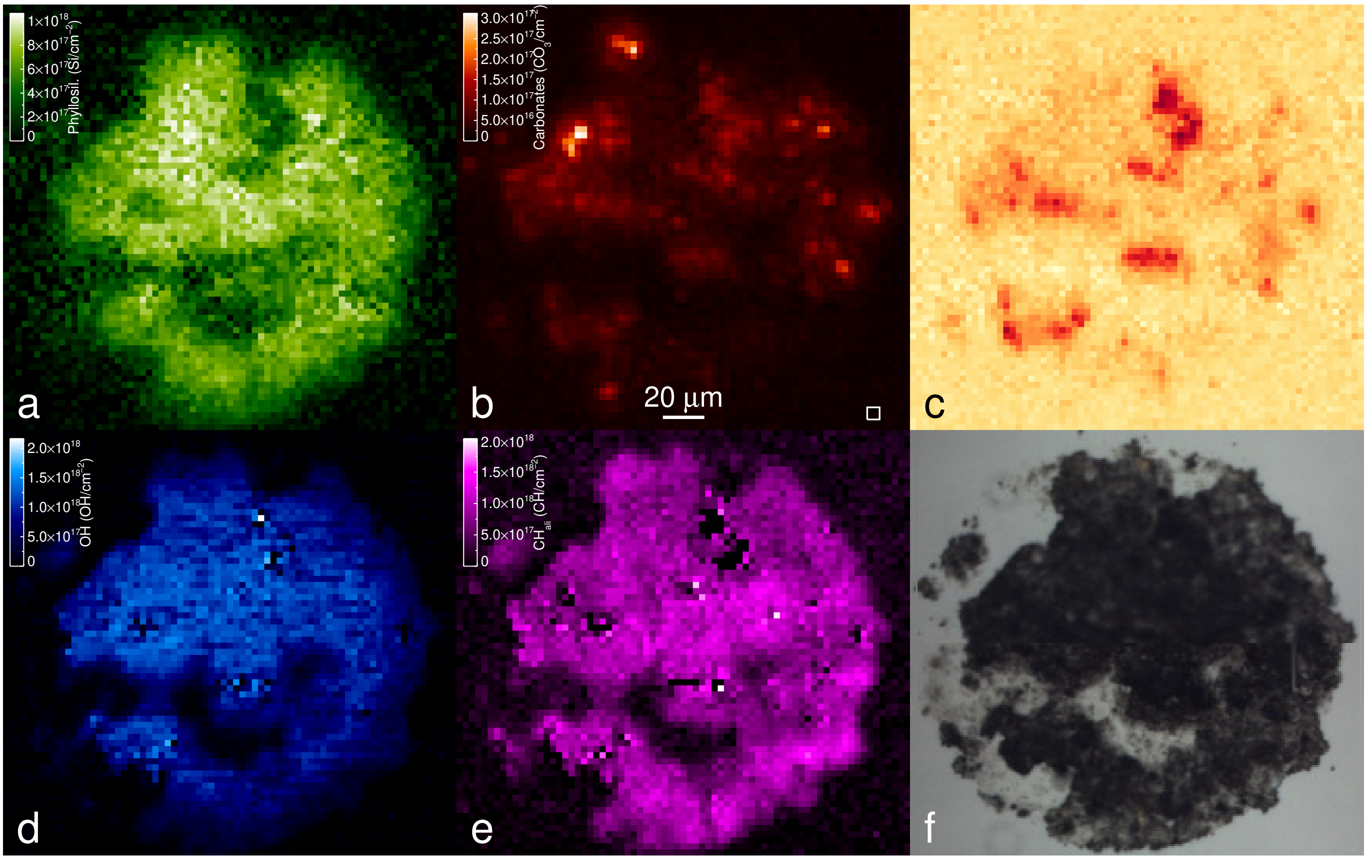

Fig. C.26: Chamber C: C0109-10-top-a

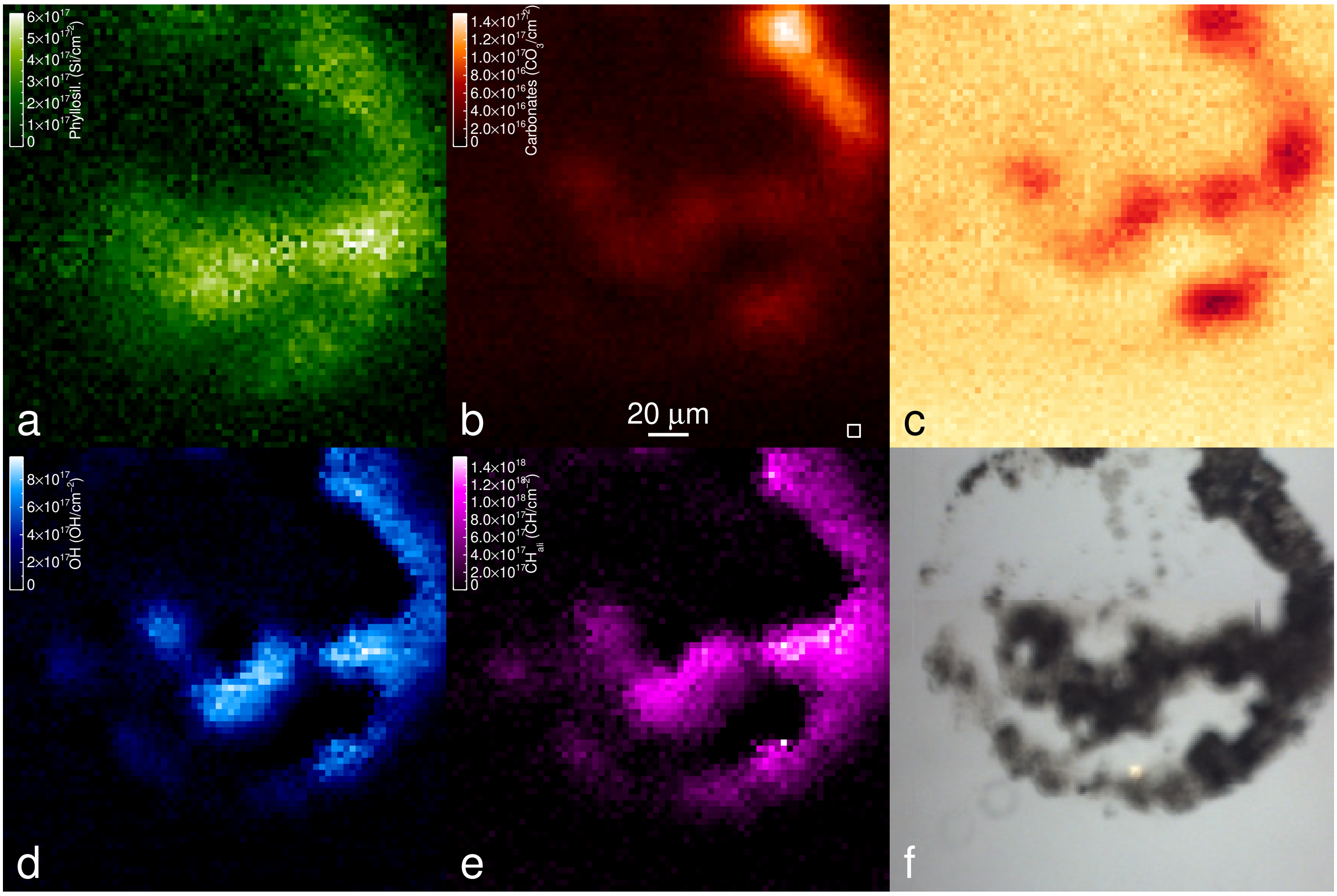

Fig. C.27: Chamber C: C0109-10-bot-a

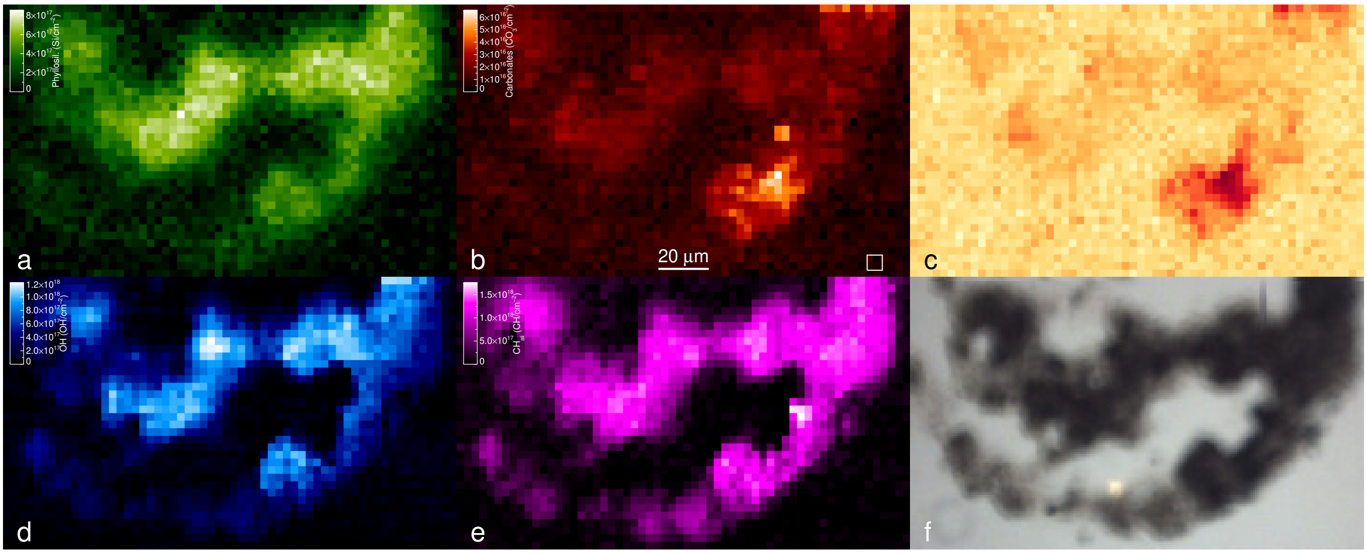

Fig. C.28: Chamber C: C0109-10 Bottom

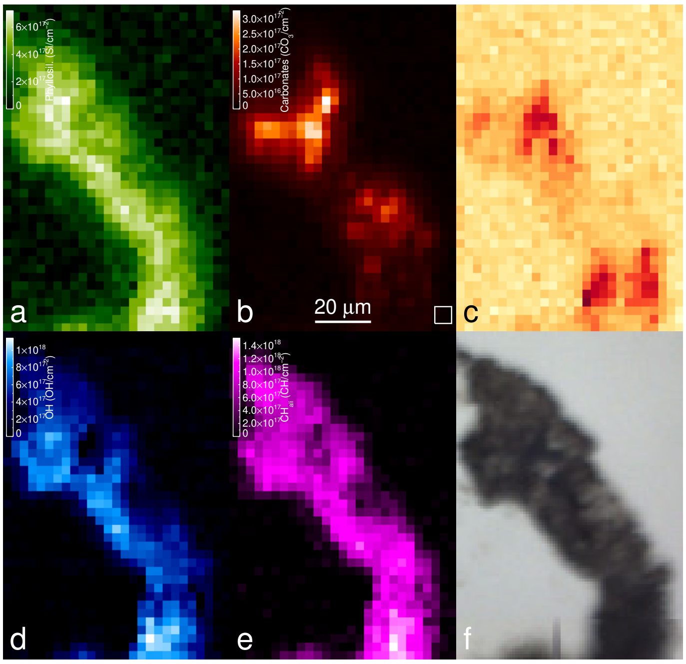

Fig. C.29: Chamber C: C0109-10 Bottom

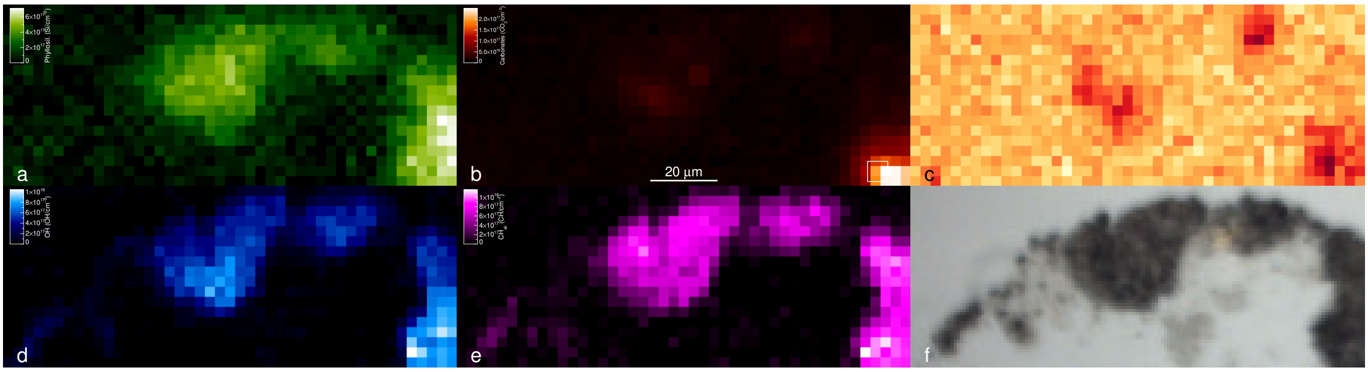

Fig. C.30: Chamber C: C0109-10 Bottom

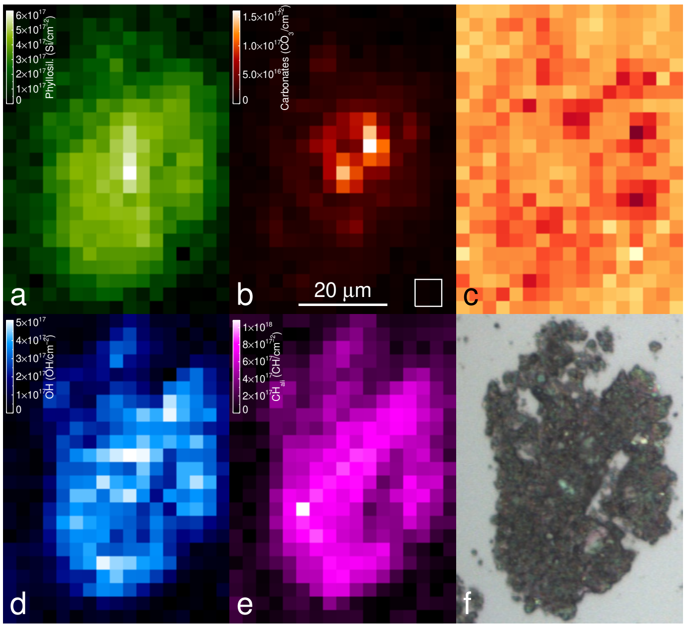

Fig. C.31: Chamber C: C0057-5-bot-a

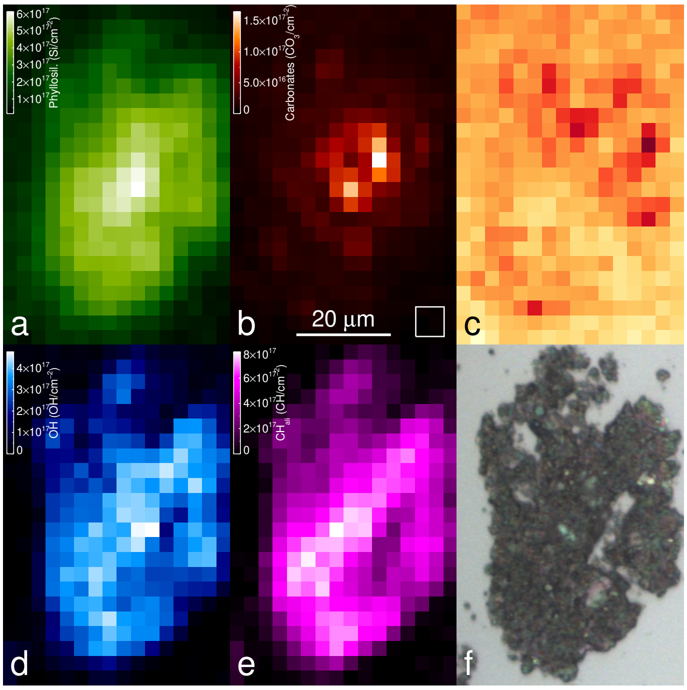

Fig. C.32: Chamber C: C0057-5-bot-b

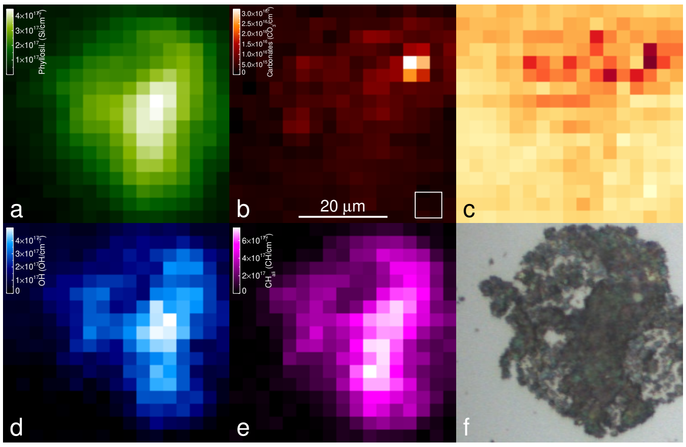

Fig. C.33: Chamber C: C0057-5-bot-c

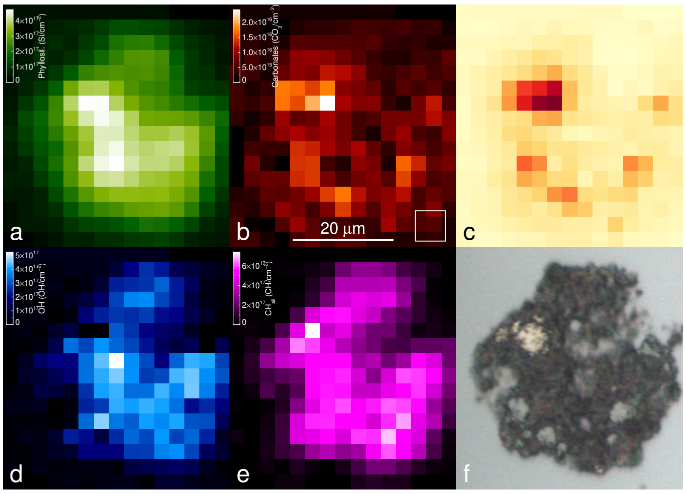

Fig. C.34: Chamber C: C0057-5-bot-d